











Publication Year	2018
Acceptance in OA@INAF	2021-02-19T16:21:01Z
Title	The 3CR Chandra Snapshot Survey: Extragalactic Radio Sources with $0.5 < z < 1.0$
Authors	MASSARO, Francesco; Missaglia, V.; Stuardi, C.; Harris, D. E.; Kraft, R. P.; et al.
DOI	10.3847/1538-4365/aa8e9d
Handle	http://hdl.handle.net/20.500.12386/30490
Journal	THE ASTROPHYSICAL JOURNAL SUPPLEMENT SERIES
Number	234



The 3CR *Chandra* Snapshot Survey: Extragalactic Radio Sources with $0.5 < z < 1.0$

F. Massaro^{1,2,3} , V. Missaglia⁴, C. Stuardi^{1,3}, D. E. Harris^{5,11} , R. P. Kraft⁵ , A. Paggi⁵ , E. Liuzzo⁶, G. R. Tremblay^{5,7} , S. A. Baum^{8,9}, C. P. O’Dea^{8,10} , B. J. Wilkes⁵ , J. Kuraszkiewicz⁵, and W. R. Forman⁵ 

¹Dipartimento di Fisica, Università degli Studi di Torino, via Pietro Giuria 1, I-10125 Torino, Italy

²Istituto Nazionale di Fisica Nucleare, Sezione di Torino, I-10125 Torino, Italy

³INAF-Osservatorio Astrofisico di Torino, via Osservatorio 20, I-10025 Pino Torinese, Italy

⁴Department of Physical Sciences, University of Napoli Federico II, via Cinthia 9, I-80126 Napoli, Italy

⁵Smithsonian Astrophysical Observatory, 60 Garden St., Cambridge, MA 02138, USA

⁶Istituto di Radioastronomia, INAF, via Gobetti 101, I-40129, Bologna, Italy

⁷Yale Center for Astronomy and Astrophysics, Physics Department, Yale University, PO Box 208120, New Haven, CT 06520-8120, USA

⁸University of Manitoba, Dept. of Physics and Astronomy, Winnipeg, MB R3T 2N2, Canada

⁹Center for Imaging Science, Rochester Institute of Technology, 84 Lomb Memorial Dr., Rochester, NY 14623, USA

¹⁰School of Physics & Astronomy, Rochester Institute of Technology, 84 Lomb Memorial Dr., Rochester, NY 14623, USA

Received 2017 March 6; revised 2017 August 15; accepted 2017 September 20; published 2018 January 12

Abstract

This paper presents the analysis of *Chandra* X-ray snapshot observations of a subsample of the extragalactic sources listed in the revised Third Cambridge radio catalog (3CR), previously lacking X-ray observations and thus observed during *Chandra* Cycle 15. This data set extends the current *Chandra* coverage of the 3CR extragalactic catalog up to redshift $z = 1.0$. Our sample includes 22 sources consisting of 1 compact steep spectrum source, 3 quasars (QSOs), and 18 FR II radio galaxies. As in our previous analyses, here we report the X-ray detections of radio cores and extended structures (i.e., knots, hotspots, and lobes) for all sources in the selected sample. We measured their X-ray intensities in three energy ranges, soft (0.5–1 keV), medium (1–2 keV), and hard (2–7 keV), and we also performed standard X-ray spectral analysis for brighter nuclei. All radio nuclei in our sample have an X-ray counterpart. We also discovered X-ray emission associated with the eastern knot of 3CR 154, with radio hotspots in 3CR 41, 3CR 54, and 3CR 225B, and with the southern lobe of 3CR 107. Extended X-ray radiation around the nuclei 3CR 293.1 and 3CR 323 on a scale of few tens of kiloparsecs was also found. X-ray extended emission, potentially arising from the hot gas in the intergalactic medium and/or due to the high-energy counterpart of lobes, is detected for 3CR 93, 3CR 154, 3CR 292, and 3CR 323 over a scale of a few hundred kiloparsecs. Finally, this work also presents an update on the state-of-the-art of *Chandra* and *XMM-Newton* observations for the entire 3CR sample.

Key words: galaxies: active – radio continuum: galaxies – X-rays: general

1. Introduction

Since the early 60s, the ensemble of extragalactic sources listed in the Third Cambridge radio catalog (3C) has represented one of the most attractive samples to study the physics of radio-loud active galactic nuclei (AGNs). Originally created using radio observations performed at 159 MHz (Edge et al. 1959), and subsequently at 178 MHz (Bennett 1962), the 3C catalog went through two main revisions later in the 80s (see, e.g., Laing et al. 1983; Spinrad et al. 1985).

Since then, a vast suite of observations became available from the radio to optical wavelengths, thus enriching the multifrequency database necessary to carry out broadband analyses. Radio images with arcsecond resolution for almost all 3CR extragalactic sources are already present in the NRAO Very Large Array (VLA) Archive Survey (NVAS)¹² and in the MERLIN¹³ archives (see, e.g., Giovannini et al. 2005). At higher frequencies, Spitzer (see, e.g., Werner et al. 2012; Dicken et al. 2014), in particular for high-redshift sources (see also Haas et al. 2008; Leipski et al. 2010), and *Hubble Space Telescope* observations cover more than 90% of the 3CR

extragalactic catalog (see e.g., Madrid et al. 2006; Privoon et al. 2008; Tremblay et al. 2009; Hilbert et al. 2016). In addition, near-infrared observations are also available for a significant fraction of the 3CR objects (see, e.g., Baldi et al. 2010). Recently, the *Herschel Space Observatory* also observed several 3CR sources, mostly focusing on the higher-redshift ones, (see e.g., Podigachoski et al. 2015; Westhues et al. 2016). Moreover, a dedicated spectroscopic campaign was carried out with the Telescopio Nazionale Galileo to provide a detailed optical classification and to study their nuclear emission (Buttiglione et al. 2009, 2011). All these observations make the extragalactic 3CR catalog an ideal sample to investigate AGN nuclear properties, extended radio structures, such as jet knots, hotspots and lobes, and/or their large-scale environments (see e.g., Ineson et al. 2013; Chiaberge et al. 2015).

However, although most of the 3CR extragalactic radio sources were observed thanks to extensive X-ray campaigns carried out with *Chandra*, *XMM-Newton*, and *Swift* (see, e.g., Hardcastle & Worrall 2000; Harvanek et al. 2001; Evans et al. 2006; Hardcastle et al. 2006; Balmaverde et al. 2012; Wilkes et al. 2013; Maselli et al. 2016, and references therein), until Cycle 9 the *Chandra* archive covered only up to $\sim 60\%$ of the 3CR extragalactic sample (see, e.g., Massaro et al. 2015, for a recent review), while the others, such as *XMM-Newton*, covered less than one-third of the entire catalog. Thus, we

¹¹ Dan Harris passed away on 2015 December 6th. His career spanned much of the history of radio and X-ray astronomy. His passion, insight, and contributions will always be remembered. A significant fraction of this work is one of his last efforts.

¹² <http://archive.nrao.edu/nvas/>

¹³ http://www.jb.man.ac.uk/cgi-bin/merlin_retrieve.pl

Table 1
Summary of the 3CR Extragalactic Sources Analyzed in Our Previous *Chandra* Investigations

Program	Cycle	Proposal Number	Number of Sources	Redshift Range	Reference
3CR snapshot survey	9	09700745	30 ^a	$z < 0.3$	Massaro et al. (2010)
XJET ^b	47	...	Massaro et al. (2011)
3CR snapshot survey	12	12700211	26	$z < 0.3$	Massaro et al. (2012)
3CR snapshot survey	13	13700190	19	$0.3 < z < 0.5$	Massaro et al. (2013)
Archival project ^b	93	...	Massaro et al. (2015)
3CR snapshot survey	15	15700111	22 ^c	$0.5 < z < 1.0$	This work

Notes.

^a The AO9 sample includes 3CR 346, which was re-observed in Cycle 12 because during Cycle 9 its *Chandra* observation was affected by high background (see Massaro et al. 2010, for details).

^b The redshift ranges for both the archival and the XJET samples are unbounded w.r.t. selection (see also <https://hea-www.harvard.edu/XJET/> for more details on the database).

^c The field of view of the 3C 255B *Chandra* observation also covers the region where 3C 255A lies, but no X-ray counterpart for its nucleus is detected.

started our *Chandra* snapshot survey to ensure that all 3CR extragalactic sources have at least an exploratory X-ray observation, with an angular resolution similar to those at lower energies, available to the astronomical community. Adopting a step-wise strategy, we requested observations in narrow redshift, z , ranges, resulting in modest proposals for each cycle to minimize the impact on the *Chandra* schedule. To date, all the 3CR sources with $z < 1$ have at least a snapshot observation (i.e., less than 20 ks total exposure time) available in the *Chandra* archive (Massaro et al. 2010, 2012, 2013) and several of them inspired follow up X-ray observations on interesting objects (see e.g., Hardcastle et al. 2010, 2012; Dasadia et al. 2016, to name a few examples).

Here, we present the analysis of the *Chandra* snapshot observations approved during Cycle 15, including all 3CR radio sources lying between $z = 0.5$ and $z = 1$ that were previously unobserved by *Chandra*.

The paper is organized as follows. The update of the ongoing *Chandra* campaign of the 3CR sources is described in Section 2 together with some details on the current sample. A brief overview of the data reduction procedures is given in Section 3, while results are described in Section 4. Then, in Section 5 we present our summary and conclusions. Finally, in the Appendix, we show X-ray images with radio contours overlaid for all the sources in the current sample (Appendix A) together with the updated summary of the *Chandra* observations for the entirety of the 3CR extragalactic catalog (Appendix B).

Unless otherwise stated, we adopt cgs units for numerical results and we also assume a flat cosmology with $H_0 = 69.6 \text{ km s}^{-1} \text{ Mpc}^{-1}$, $\Omega_M = 0.286$, and $\Omega_\Lambda = 0.714$ (Bennett et al. 2014). Spectral indices, α , are defined by flux density, $S_\nu \propto \nu^{-\alpha}$.

2. State-of-the-art of the 3CR Extragalactic *Chandra* Snapshot Survey

The revised 3C extragalactic catalog includes 298 sources (Spinrad et al. 1985). We have already analyzed and published all the data collected to date for the *Chandra* observations carried out in Cycles 9, 12, and 13 for a total of 75 sources (Massaro et al. 2010, 2012, 2013), and an additional 140 objects, listed in the *Chandra* archive, were also presented, adopting the same data reduction procedures (Massaro et al. 2011, 2015). Several subsets of the 3CR sample have also been observed by other groups

(e.g., Wilkes et al. 2013; Kuraszkiewicz et al. 2017). Table 1 summarizes the references for the *Chandra* observations of the 3CR extragalactic sources already analyzed and published as part of this compilation.

In our previous archival analyses we excluded seven sources, namely 3CR 66A (e.g., Abdo et al. 2011), 3CR 71 (alias NGC 1068; e.g., Brinkman et al. 2002), 3CR 84 (alias NGC1275 or Perseus A; e.g., Fabian et al. 2003), 3CR 186 (Siemiginowska et al. 2010), 3CR 231 (alias M82; e.g., Griffiths et al. 2000), 3CR 317 (alias Abell 2052; e.g., Blanton et al. 2009), and 3CR 348 (alias Hercules A; e.g., Nulsen et al. 2005), since each of these source has accumulated an exposure time of greater than 80 ks, and has been discussed extensively in the literature. In addition, we also did not re-analyze: 3CR 236, 3CR 326, 3CR 386, since the PI of these observations is currently carrying out the analysis (M. Birkinshaw 2017, private communication).

The *Chandra* archive now includes all the 3CR extragalactic sources up to $z = 0.5$ (i.e., 150 sources), with the only exceptions being those objects for which spectroscopic observations, performed after the last revision (Spinrad et al. 1985), reported different redshift estimates, namely: 3CR 27, at $z = 0.184$, 3CR 69 at $z = 0.458$ (Hiltner & Roeser 2009), and 3CR 93 at $z = 0.357$, as confirmed by Ho & Minjin (2009). The present analysis extends the *Chandra* database up to $z = 1.0$, including 22 more targets. During these Cycle 15 3CR snapshot observations, we also observed 3CR 142.1 and 3CR 277, for which the redshift reported in the literature (Hewitt & Burbidge 1991) updates the earlier estimates from Spinrad et al. (1985). These two sources, together with 3CR 93, belong to the sample of 22 targets analyzed in the present work. *Chandra* snapshot observations of 3CR 27 and 3CR 69 were proposed and obtained in subsequent observing cycles (Stuardi et al. 2017).

Of the 298 3CR extragalactic sources, 25 are still unidentified, lacking the optical counterpart and/or an optical spectroscopic observation necessary to unveil their nature. We recently observed 21 of these 25 targets with *Swift* snapshot observations, discovering X-ray counterparts for 11 of them, but even using optical data available thanks to the instruments on board the *Swift* satellite, we could not discern and/or confirm their extragalactic nature (see Maselli et al. 2016 for all details).

A summary table on the state-of-the-art of the *Chandra* observations for all the 3CR extragalactic sources, including detections of extended components: jet knots, hotspots, lobes, and

Table 2
Source List of the *Chandra* AO15 Snapshot Survey

3CR name	Class	R.A. (J2000) (hh mm ss)	Decl. (J2000) (dd mm ss)	z	kpc scale (kpc/arcsec)	D_L (Mpc)	N_H cm^{-2}	m_v	S_{178} Jy	<i>Chandra</i> Obs. ID	Obs. Date yyyy mm dd
34	FR II—HERG	01 10 18.542	+31 47 19.51	0.69	7.191	4236.3	5.50e20	21	11.9	16046	2014 Sep 25
41	FR II—HERG	01 26 44.325	+33 13 10.96	0.794	7.586	5035.7	5.09e20	21	10.6	16047	2014 Sep 03
44	QSO	01 31 21.647	+06 23 43.14	0.66	7.058	4011.6	3.18e20	22	7.9	16048	2014 Jun 14
54	FR II—HERG	01 55 30.258	+43 45 59.06	0.8274	7.693	5298.7	7.80e20	22	8.8	16049	2014 Jun 15
55	FR II—HERG	01 57 10.539	+28 51 39.70	0.735	7.374	4578.4	5.38e20	22	21.5	16050	2014 Jun 15
93	QSO	03 43 29.996	+04 57 48.60	0.358	5.059	1924.5	1.15e21	18.1	9.9	16051	2014 Oct 10
107	FR II—HERG	04 12 22.620	−00 59 32.69	0.785	7.555	4965.3	8.42e20	22	10.8	16052	2014 Sep 02
114	FR II—LERG	04 20 22.243	+17 53 56.97	0.815	7.654	5200.7	1.61e21	22	6.5	16053	2014 Sep 02
142.1	FR II	05 31 29.334	+06 30 26.90	0.4061	5.476	2233	1.79e21	21	19.4	16054	2014 Aug 16
154	QSO	06 13 50.139	+26 04 36.64	0.580	6.654	3426.3	3.47e21	18.0	23.1	16055	2014 Aug 13
169.1	FR II—HERG	06 51 14.816	+45 09 28.56	0.633	6.930	3811.7	9.30e20	20.5	7.3	16056	2014 Aug 16
217	FR II—HERG	09 08 50.6	+37 48 19	0.898	7.892	5863.9	1.68e20	22	11.3	16057	2014 Jun 13
225B	FR II—HERG	09 42 15.396	+13 45 50.49	0.582	6.665	3440.7	3.45e20	19	21.3	16058	2014 Oct 18
237	FR II—CSS	10 08 00.0	+07 30 16	0.877	7.836	5694.5	1.89e20	21	20.9	16059	2014 Oct 31
247	FR II—HERG	10 58 58.973	+43 01 24.66	0.750	7.430	4693.7	8.79e19	21.5	10.6	16060	2014 Sep 26
272	FR II	12 24 28.5	+42 06 36	0.944	8.003	6238.6	2.23e20	22	8	16061	2015 Mar 01
277	FR II	12 51 43.6	+50 34 25	0.414	5.540	2284.7	1.04e20	20	7.5	16062	2015 Mar 03
277.2	FR II—HERG	12 53 33.330	+15 42 31.18	0.767	7.492	4825.2	1.70e20	21.5	12	16063	2015 Apr 07
288.1	QSO	13 42 13.267	+60 21 42.79	0.9610	8.041	6378.3	1.75e20	18.1	9	16064	2014 Jun 08
292	FR II—HERG	13 50 41.852	+64 29 35.86	0.713	7.287	4410.4	1.66e20	20.7	10.1	16065 ^a	2014 Sep 12
293.1	FR II	13 54 40.519	+16 14 43.14	0.709	7.271	4380.0	1.82e20	21	9.2	16066	2014 Jun 05
323	FR II	15 41 45.594	+60 15 34.03	0.6790	7.143	4153.6	1.49e20	21	8.4	16067	2014 Apr 30

Note. Column (1): the 3CR name. Column (2): the “class” column contains both a radio descriptor (Fanaroff–Riley class I or II), Compact Steep Spectrum (CSS) and the optical spectroscopic designation, LERG, “Low Excitation Radio Galaxy,” HERG, “High Excitation Radio Galaxy,” and QSO for quasars (see also Perryman et al. 1984; Hes et al. 1996; Grimes et al. 2004, for more details). Columns (3)–(4): the celestial positions listed are those of the radio nuclei that we used to register the X-ray images: right ascension and declination (equinox J2000, see Section 3 for details). We reported here the original 3CR position (Spinrad et al. 1985) of the sources for which the radio core was not clearly detected. Column (5): redshift z . We also verified in the literature (e.g., NED and/or SIMBAD databases) if new z values were reported after the release of the 3CR catalog. Column (6): the angular to linear scale factor in arcseconds. Cosmological parameters used to compute it are reported in Section 1. Column (7): luminosity distance in Mpc. Cosmological parameters used to compute it are reported in Section 1. Column (8): galactic neutral hydrogen column densities N_H along the line of sight (Kalberla et al. 2005). Col. (9): the optical magnitude in the V band taken from the 3CR catalog (Spinrad et al. 1985). Column (10): S_{178} is the flux density at 178 MHz, taken from Spinrad et al. (1985). Column (11): the *Chandra* observation ID. Column (12): the date when the *Chandra* observation was performed.

^a For 3CR 292, two *Chandra* observations are available with obsID 16065 and 17488, the latter performed in 2014 Nov 21, (see Section 4 for details).

X-ray emission from the hot intergalactic medium present in galaxy groups/clusters, is reported in Appendix B.

3. Data Reduction and Data Analysis

Data reduction and analysis procedures adopted for all the *Chandra* observations presented here were extensively described in our previous papers, thus only a brief overview is reported in the following. We adopted the same procedures, since our final aim is to create a uniform database for the entire 3CR extragalactic survey once all the sources listed therein will be observed by *Chandra*.

We followed the standard procedure described in the *Chandra* Interactive Analysis of Observations (CIAO) threads¹⁴ to perform our data reduction, and we used CIAO v4.7 with the *Chandra* Calibration Database (CALDB) version 4.6.2. The log of *Chandra* observations is reported in Table 2.

3.1. X-Ray Photometry

We initially generated level two event files using the *acis_process_events* task and filtering for grades 0,2,3,4,6. We checked the absence of high background intervals,

inspecting the light curves extracted for each data set, but this never occurred. We aligned the X-ray position of each core with that of the radio to perform the astrometric registration (see, e.g., Massaro et al. 2011, for details). The source 3CR 292 has been observed twice with *Chandra* (obsID 16065 and obsID 17488, with exposure times of ~ 4 ks and ~ 8 ks, respectively). In this case, a merged event file was created using the CIAO routine REPROJECT_OBS, thus reprojecting event files to the reference coordinates of the deeper observation (i.e., obsID 17488).

Then we created flux maps in the X-ray energy ranges, 0.5–1 keV (soft), 1–2 keV (medium), 2–7 keV (hard), taking into account exposure time and effective area. In our procedure, as previously done, we used monochromatic exposure maps set to the nominal energies of 0.75, 1.4, and 4 keV for the soft, medium, and hard bands, respectively. All flux maps were converted from units of counts $\text{s}^{-1} \text{cm}^{-2}$ to cgs units by multiplying each event by the nominal energy of each band. However, we made the necessary correction to recover the observed $\text{erg cm}^{-2} \text{s}^{-1}$, when performing X-ray photometry (see, e.g., Massaro et al. 2009a, 2009b, for details).

We measured observed fluxes for all the X-ray detected nuclei and extended components. This was done by choosing a region of size and shape appropriate to the observed X-ray emission and

¹⁴ <http://cxc.harvard.edu/ciao/guides/index.html>

Table 3
X-Ray Emission from Radio Cores

3CR name	Ext. Ratio	$F_{0.5-1 \text{ keV}}^a$ (cgs)	$F_{1-2 \text{ keV}}^a$ (cgs)	$F_{2-7 \text{ keV}}^a$ (cgs)	$F_{0.5-7 \text{ keV}}^a$ (cgs)	L_X ($10^{44} \text{ erg s}^{-1}$)
34	0.72 (0.04)	0.25 (0.57)	4.69 (1.43)	77.53 (9.95)	82.47 (10.06)	1.76 (0.22)
41	0.59 (0.06)	0.32 (0.32)	0.94 (0.68)	41.33 (7.42)	42.6 (7.46)	1.29 (0.23)
44	0.45 (0.09)	0.82 (0.59)	0.68 (0.64)	9.71 (3.67)	11.22 (3.77)	0.22 (0.07)
54	0.83 (0.05)	1.06 (0.75)	4.76 (1.33)	41.04 (7.25)	46.85 (7.41)	1.57 (0.25)
55	0.48 (0.09)	0.82 (0.58)	2.41 (0.91)	8.39 (3.47)	11.61 (3.64)	0.29 (0.09)
93	0.948 (0.006)	77.48 (6.26)	157.41 (7.41)	429.53 (22.58)	664.42 (24.58)	2.94 (0.11)
107	0.15 (0.06)	0.38 (0.38)	0.49 (0.49)	2.95 (2.12)	3.82 (2.21)	0.11 (0.07)
114	0.91 (0.02)	1.16 (0.82)	43.23 (4.05)	255.54 (17.3)	299.94 (17.78)	9.71 (0.58)
142.1	0.61 (0.09)	0.57 (0.57)	2.24 (0.91)	11.19 (3.77)	13.99 (3.92)	0.08 (0.02)
154	0.947 (0.006)	41.35 (4.59)	241.5 (9.31)	923.47 (33.73)	1206.32 (35.29)	16.95 (0.5)
169.1	0.64 (0.08)	2.1 (0.94)	0.23 (0.51)	18.65 (4.98)	20.98 (5.1)	0.36 (0.09)
217	0.91 (0.20)	1.42 (1.0)	15.01 (2.29)	100.01 (10.98)	116.44 (11.26)	4.78 (0.46)
225B	0.48 (0.11)	0.68 (0.48)	0.12 (0.26)	5.18 (2.59)	5.98 (2.65)	0.08 (0.04)
237	0.84 (0.05)	4.11 (1.45)	7.0 (1.53)	13.76 (4.01)	24.87 (4.53)	0.97 (0.18)
247	0.7 (0.06)	0.99 (0.7)	3.71 (1.25)	36.22 (6.61)	40.92 (6.77)	1.07 (0.18)
272	0.41 (0.12)	0.0 (0.0)	0.46 (0.46)	4.85 (2.48)	5.31 (2.52)	0.25 (0.12)
277	0.84 (0.06)	0.33 (0.33)	2.2 (1.0)	26.81 (6.0)	29.34 (6.09)	0.18 (0.04)
277.2	0.43 (0.10)	3.15 (1.29)	0.21 (0.47)	2.26 (2.26)	5.63 (2.65)	0.16 (0.07)
288.1	0.946 (0.08)	76.35 (5.65)	114.05 (6.1)	236.49 (16.45)	426.88 (18.43)	20.78 (0.9)
292	0.86 (0.04)	0.9 (0.9)	1.8 (1.04)	103.58 (14.13)	106.29 (14.19)	2.47 (0.33)
293.1	0.26 (0.10)	0.0 (0.0)	0.84 (0.6)	1.76 (1.24)	2.59 (1.38)	0.06 (0.03)
323	0.18 (0.06)	0.0 (0.0)	0.9 (0.65)	5.03 (2.25)	5.93 (2.34)	0.12 (0.05)

Notes. Column (1): the 3CR name. Column (2): the Ext. Ratio defined as the ratio of the net counts in the $r = 2''$ circle to the net counts in the $r = 10''$ circular region surrounding the core of each 3CR source. The 1σ uncertainties are given in parenthesis. Column (3): measured X-ray flux between 0.5 and 1 keV. Column (4): measured X-ray flux between 1 and 2 keV. Column (5): measured X-ray flux between 2 and 7 keV. Column (6): measured X-ray flux between 0.5 and 7 keV. Column (7): X-ray luminosity in the range 0.5–7 keV with the 1σ uncertainties given in parenthesis.

^a Fluxes are given in units of $10^{-15} \text{ erg cm}^{-2} \text{ s}^{-1}$ and 1σ uncertainties are given in parentheses. The uncertainties on the flux measurements are computed as described in Section 3.

^b Sources with count rates above the threshold of 0.1 counts per frame for which the X-ray flux measurement is affected by pileup (see Massaro et al. 2013, and references therein for additional details).

matching the radio structure. We also chose two background regions with the same shape and size so as to avoid X-ray emission from other parts of the source. The flux for each energy band and region was measured using funtools,¹⁵ as in our previous analyses. Uncertainties are computed assuming Poisson statistics (i.e., square root of the number of counts) in the source and background regions. X-ray fluxes, not corrected for the Galactic absorption, but measured for the cores, are reported in Table 3, while those for detected jet knots, hotspots, and lobes are given in Table 5. The name of each component (e.g., knot or hotspot) is a combination of one letter indicating the orientation of the radio structure and one number indicating distance from the core in arcseconds.

Since the *Chandra* native pixel size for the ACIS instrument is $0''.492$, the data are undersampled, thus to recover the resolution we regridded our images to 1/2, 1/4, or 1/8 of the native ACIS pixel size. This was dictated by the angular size of each radio source and by the number of counts in each source component. For sources of large angular extent, 1/2 or no regridding was adopted (see also Massaro et al. 2012, 2013, for more details).

Finally, we performed a comparison between radio and X-ray images at similar angular resolution to verify if extended structures in radio sources, such as jet knots, hotspots, and lobes, have an X-ray counterpart. To achieve this goal, we used radio images retrieved from publicly available websites such as that

¹⁵ <https://github.com/ericmandel/funtools>

Table 4

Results of the X-Ray Spectral Analysis for the Brighter Nuclei

3CR	Γ_X	$N_{H,int}$	F	χ^2/dof
93	1.78(−0.08, 0.15)	<0.06	<0.91	34.91/25
114	2.06(−0.34, 0.36)	7.21(−2.4, 2.54)	...	3.91/7
154	1.85(−0.14, 0.18)	0.61(−0.26, 0.28)	<0.92	41.52/39
288.1	1.77(−0.08, 0.09)	<0.1	...	16.99/19

Note. Column (1): the 3CR name. Column (2): the X-ray photon index Γ_X . Column (3): the intrinsic absorption at the source redshift. Column (4): the fraction of flux falling into the pileup region. Column (5): the χ^2 value divided by the degrees of freedom. The quoted statistical uncertainties refer to the 68% confidence level.

of the National Radio Astronomy Observatory VLA Archive Survey (NVAS),¹⁶ NASA Extragalactic Database (NED),¹⁷ and the (DRAGN)¹⁸ website, as well as the personal websites of our colleagues.^{19,20} Image parameters for each radio observation used are given in the figure captions of Appendix A. X-ray fluxes for the high-energy counterparts of the radio nuclei are reported in Table 3.

¹⁶ <http://archive.nrao.edu/nvas/>

¹⁷ <http://ned.ipac.caltech.edu/>

¹⁸ <http://www.jb.man.ac.uk/atlas/>

¹⁹ <http://3cr.extragalactic.info>

²⁰ <http://www.slac.stanford.edu/~teddy/vla3cr/vla3cr.html>

Table 5
X-Ray Emission from Radio Extended Structures (i.e., Knots and Hotspots)

3CR name	Component	Class	Counts	$F_{0.5-1 \text{ keV}}^a$ (cgs)	$F_{1-2 \text{ keV}}^a$ (cgs)	$F_{2-7 \text{ keV}}^a$ (cgs)	$F_{0.5-7 \text{ keV}}^a$ (cgs)	L_X ($10^{42} \text{ erg s}^{-1}$)
41	s11.3	h	6 (0.1)	0.56 (0.56)	0.55 (0.55)	4.7 (2.7)	5.8 (2.8)	17.5 (8.5)
54	s9.3	h	3 (0.4)	0.0 (0.0)	0.91 (0.52)	0.0 (0.0)	0.91 (0.52)	3.05 (1.74)
107	s5.0	l	11 (1.5)	0.62 (0.62)	1.3 (0.8)	3.9 (2.3)	5.9 (2.5)	17.3 (7.2)
154	e33.0	k	8 (0.9)	0.0 (0.0)	<0.24	6.3 (2.6)	6.6 (2.6)	9.2 (3.7)
225B	w2.0	h	4 (0.1)	0.0 (0.0)	0.79 (0.58)	0.69 (0.69)	1.5 (0.9)	2.1 (1.3)

Note. Column (1): the 3CR name. Column (2): the component name (e.g., knot or hotspot) is a combination of one letter indicating the orientation of the radio structure and one number indicating the distance from the core in arcseconds. Column (3): the component class: “h” = hotspot, “k” = knot, “l” = lobe. Column (4): the total counts in the photometric circle together with the average of the eight background regions, in parentheses, both for the 0.5 to 7 keV band. Column (5): measured X-ray flux between 0.5 and 1 keV. Column (6): measured X-ray flux between 1 and 2 keV. Column (7): measured X-ray flux between 2 and 7 keV. Column (8): measured X-ray flux between 0.5 and 7 keV. Column (9): X-ray luminosity in the range 0.5 to 7 keV, with the 1σ uncertainties given in parentheses.

^a Fluxes are given in units of $10^{-15} \text{ erg cm}^{-2} \text{ s}^{-1}$ and 1σ uncertainties are given in parentheses. The uncertainties on the flux measurements were computed as described in Section 3.

3.2. X-Ray Spectral Analysis

We performed spectral analysis for the X-ray counterparts of radio cores of those sources with more than 400 counts to determine their X-ray spectral indices α_X , the presence or absence of significant intrinsic absorption, and the role played by mild pileup in artificially hardening the spectrum.

The spectral data were extracted from a $2''$ aperture for photometric measurements, using the CIAO routine SPECEXTRACT, thereby automating the creation of count-weighted response matrices. Background spectra were extracted in nearby circular regions of radius $10''$ not containing obvious sources. The source spectra were then filtered in energy between 0.5 and 7 keV and binned to allow a minimum number of 30 counts per bin to ensure the use of the Gaussian statistic. We used the SHERPA²¹ modeling and fitting package to fit our spectra. For each source we adopted two models: (1) a redshifted power law with Galactic and intrinsic photoelectric absorption components, and (2) the same model with an additional pileup component using the JDPILEUP *Chandra* CCD pileup model developed by Davis (2001).

Prior to fitting, the Galactic hydrogen column density and the source redshift were fixed at the measured values for each source. When considering the first (1) fitting model, the two main variable parameters—namely the intrinsic absorption ($N_H(z)$) and X-ray photon index Γ —were allowed to vary in a first pass fit, but subsequently stepped through a range of possible physical values to explore the parameter space, determine 68% confidence intervals, and quantify the degree to which $N_H(z)$ and Γ are degenerate.

We have also explored the possible effect of pileup on our sources by adding a JDPILEUP²² component to our baseline model (2). We left the parameters of the JDPILEUP model fixed to their default values, with the exception of ALPHA (the probability of a good grade when two photons pile together) and F (the fraction of flux falling into the pileup region). In no case were we able to constrain the value of ALPHA since it was usually degenerate with F and/or the intrinsic absorption, so we decided to freeze it to its default value of 1. The value of F was left free to vary between 0.85

and 1, and was constrained in two cases. The results of spectral fitting are given in Table 4.

4. Results

4.1. General

We detected the X-ray counterpart of all radio cores in our sample and we measured their fluxes, adopting a circular region of $2''$ centered on the radio position used for the astrometric registration. All the results of our X-ray photometry, i.e., nuclear X-ray fluxes in the three different bands (see Section 3), together with their X-ray luminosities, are reported in Table 3, while X-ray images for the whole selected sample are presented in Appendix A. In Table 3, we also report the values of the “extended emission” parameter, computed as the ratio of the total number of counts in a circular region of radius $r = 2''$ circle to that of a circle of radius $r = 10''$, both centered on the radio position of each 3CR source (i.e., Ext. Ratio “Extent Ratio”). This ratio is close to unity for unresolved (i.e., point-like) sources, since the on-axis encircled energy for $2''$ is $\simeq 0.97$, and only a small increase is expected up to $10''$. Thus, parameter values significantly less than 0.9 indicate the presence of extended emission around the nuclear component (e.g., Massaro et al. 2010, 2013). In our sample this situation clearly occurs for 3CR 107, 3CR 293.1, and 3CR 323.

Of the 22 sources, 4 of them, namely 3CR 93, 3CR 114, 3CR 154, and 3CR 288.1, show X-ray nuclei with more than 400 counts within a circular region of $2''$ radius. Thus, according to our previous works, we performed a basic X-ray spectral analysis for them. Their spectra are consistent with a mildly absorbed power law with absorption consistent with the Galactic value (Kalberla et al. 2005). 3CR 93 and 3CR 154 show a fraction of pileup of 10%; however, their fits do not improve significantly when including a jdpileup spectral component²³. Results of the spectral analysis are reported in Table 4, and the quoted statistical uncertainties refer to the 68% confidence level.

We also discovered X-ray emission associated with three hotspots in three different sources; their X-ray fluxes are reported in Table 5 together with detection significances, all above 3σ , computed assuming a Poisson distribution for the

²¹ <http://cxc.harvard.edu/sherpa>

²² <http://cxc.harvard.edu/sherpa/ahelp/jdpileup.html>

²³ <http://cxc.harvard.edu/sherpa/ahelp/jdpileup.html>

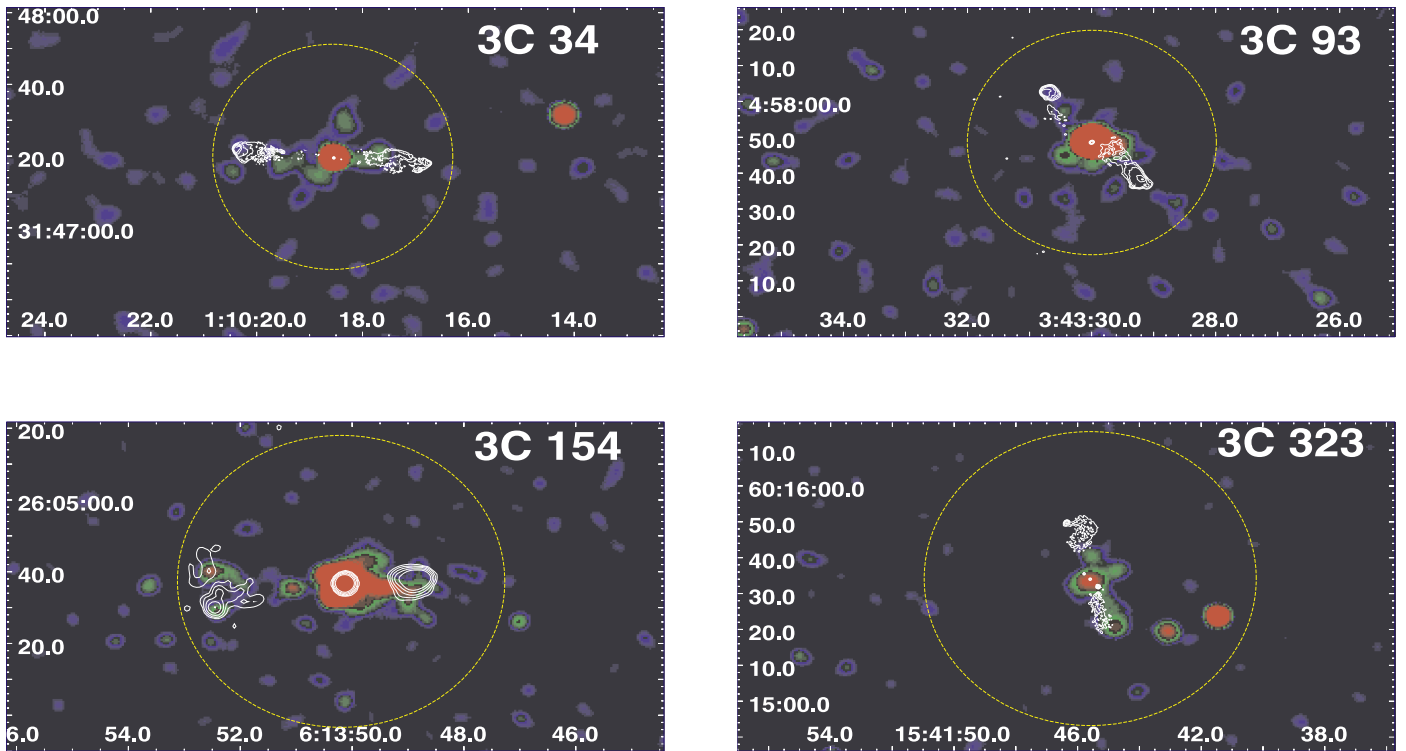


Figure 1. *Chandra* X-ray images for 3CR 34 (top left), 3CR 93 (top right), 3CR 154 (bottom left), and 3CR 323 (bottom right) in the energy range 0.5–7 keV. Event files have not been regridded. Images are all smoothed with a Gaussian function of 8-pixel kernel radius. The five radio contour levels (white) overlaid on the *Chandra* image were computed starting at 0.2, 0.4, 2, and 0.3 mJy/beam, increasing by a factor of 2, respectively. The radio maps adopted to perform the comparison with the X-ray images are the same used for the registration and shown in Appendix A. A circular region of similar size to the radio structure, centered at the position of the radio cores and having radii of 30'' for 3CR 34 and 3CR 93 and 40'' for 3CR 154 and 3CR 323, respectively, is marked with a dashed yellow line. An excess of X-ray counts, greater than 2σ for 3CR 34 and greater than 3σ for the others, is detected. This could be due to the presence of hot gas filling their large-scale X-ray environments, but it could also be contaminated by the radiation arising from the lobes of these FR II radio galaxies being aligned with their large-scale radio structure.

background. The X-ray counterpart of a radio knot in the 3CR 154 eastern lobe and the counterpart of the whole southern radio lobe of 3CR 107 were also found (see Table 5 for details).

Of the 22 3CR sources in our sample, 3 lie within an optically known galaxy cluster, namely: 3CR 34, 3CR 44, and 3CR 247 (Spinrad et al. 1985) and to search for possible X-ray emission due to the hot gas permeating the intergalactic medium around the radio structure, we adopted the following procedure for all our targets. We measured the total number of counts in a circular region with diameter equal to the total extent of the radio source and we subtracted those counts within circular regions of 2'' corresponding to the radio nucleus and/or to background sources lying within the larger circle. Then, assuming a Poisson distribution for the background events, we computed the probability of obtaining the measured value given the expected number of counts in the background.

We detected an excess of X-ray photons, above 3σ significance, around the radio structures of 3CR 93, 3CR 154, and 3CR 323, on a scale of a few hundred kiloparsecs as shown in Figure 1. Such X-ray extended emission could be due to the presence of hot gas filling their large-scale X-ray environment (see Figure 1), but it could also be contaminated by the radiation arising from the lobes of these FR II radio galaxies,

which would be aligned with their large-scale radio structure. These scenarios are indistinguishable due to the low number of counts available, but we tend to favor the former (i.e., the presence of hot gas in the intergalactic medium) since the peaks of the X-ray surface brightness do not appear to be coincident with those of the radio intensity (i.e., hotspots in the lobes). We also found a marginal detection (i.e., 2σ significance) of X-ray emission from the group/cluster around 3CR 34 (see also Figure 1). For this source we do not claim that the extended X-ray emission could be associated with the radio lobes because it lies in a galaxy-rich large-scale environment (McCarthy et al. 1995). Then we also discovered extended X-ray emission for 3CR 292 on scale of hundred of parsecs (see Figure 2) above 3σ significance. Here, an excess of X-ray photons is also found to be associated with the northern hotspot/lobe, but it is consistent with a 3σ fluctuation of the X-ray diffuse background (more details are given in the following section). A specific analysis to search for galaxy groups or cluster signatures surrounding the 3CR sources observed during the *Chandra* snapshot survey is out of the scope of this paper and will be presented in a forthcoming work.

Finally, the X-ray images with radio contours overlaid for all the sources in the current sample are shown in Appendix A.

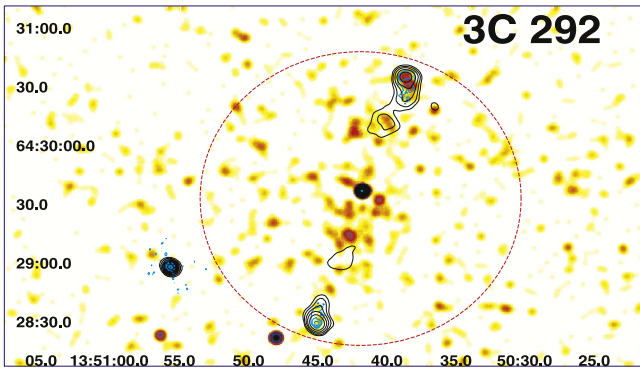


Figure 2. *Chandra* X-ray image for 3CR 292 in the energy range 0.5–7 keV. The merged event file has been created by combining both observations available in the archive (obsID 16065 and obsID 17488, ~ 4 ks and ~ 8 ks exposure time, respectively). The X-ray image has been smoothed with a Gaussian function of 8-pixel kernel radius. The five radio contour levels, black at 1.4 GHz and cyan at 8.5 GHz, overlaid on the *Chandra* image, were computed starting at 8 mJy/beam and 0.4, increasing by a factor of 2 and 4, respectively. The radio map at 1.4 GHz is not registered because the radio core is undetected.

4.2. Source Details

3CR 34. This is an FR II radio galaxy at $z = 0.69$ and is optically classified as a high-excitation line radio galaxy (HERG; Mullin et al. 2006). It lies near the center of a compact cluster of galaxies (McCarthy et al. 1995), appearing as one of the reddest members and surrounded by fainter companions. There is a double hotspot in the western lobe. Best et al. (1997) reported the detection of a strong jet-cloud interaction at 120 kpc from the core and *HST* images also show a narrow region of blue emission oriented along the radio axis and directed toward a radio hotspot. In the *Chandra* observation analyzed here we only detected the X-ray core. We tested the presence of diffuse X-ray emission due to the intergalactic medium of the known galaxy cluster where 3C 34 lies according to the procedure previously described. We found an X-ray excess of about 3σ significance (see Figure 1) where the number of counts in an annular region of radii $2''$ and $30''$, centered on the radio core position, is 90, compared with 45.7 expected background counts in that region. We also estimated the luminosity of the X-ray extended emission, L_X , adopting an annular region of inner radius $2''$ and outer radius $30''$, centered on the position of the 3CR 34 radio nucleus, to exclude the nuclear contribution of the central radio galaxy. Our estimate is $L_X = (5.2 \pm 2.2) \times 10^{43}$ erg s $^{-1}$. We note that this L_X estimate, as in the following cases of 3CR 93, 3CR 154, 3CR 292, and 3CR 323, is an upper limit on the X-ray luminosity of the hot gas in the intergalactic medium, since there could be a possible contamination due to the lobe X-ray emission.

3CR 41. This is an FR II radio galaxy with $z = 0.79$, classified as a narrow emission line radio galaxy. In the radio image at 8.45 GHz there is no detection of a jet in the northern lobe, while extended radio emission associated with the jet pointing toward the southeastern hotspot is detected (Mullin et al. 2008, see e.g.). Both radio lobes are also visible even at 8.45 GHz. At higher energies, in our *Chandra* snapshot observations, the southern hotspot is detected, as well as the core of the radio galaxy.

3CR 44. This quasar, with a radio morphology similar to that of an FR II radio galaxy, is at $z = 0.66$ and is associated with a galaxy cluster visible in the optical image (O’Dea et al. 2009). Kharb et al. (2008) reported the hint of a jet-like structure extending toward the southern hotspot in the 5 GHz radio map, while the *HST* image shows this radio galaxy to be either composed of two structures oriented north–south, or, more likely, bisected by a dust lane running east–west (McCarthy et al. 1997). We clearly detected the nuclear emission in the X-rays and we also found an excess of X-ray counts associated with the northern lobe but at $<3\sigma$ significance.

3CR 54. This is an FR II radio galaxy at redshift $z = 0.8274$. The lobe morphology on the southern side of the source is more extended than the northern one (Kharb et al. 2008). In the *HST* image, the galaxy has close companions and the source appears extended toward the southwest side, but it is unclear if it is a bridge, a tidal tail, or a jet feature (McCarthy et al. 1997). In the X-ray image the radio core is clearly detected, together with the southern hotspot.

3CR 55. This is an FR II radio galaxy at $z = 0.735$ and is optically classified as a narrow emission line radio galaxy. The radio core is detected in the X-rays, while the two hotspots are not.

3CR 93. This is a $z = 0.358$ quasar with a lobe-dominated radio morphology (see, e.g., Bogers et al. 1994). In the optical image, available in the *HST* archive, 3CR 93 has a host galaxy with $\sim 3''$ diameter (Lehnert et al. 1999). In the X-ray image the core is clearly detected with more than 1000 counts but there is no detection of hotspots. X-ray spectral analysis of the nuclear emission shows a power-law spectrum with absorption consistent with the Galactic column density. Significant extended X-ray emission on a scale of hundreds of kiloparsecs was found around 3CR 93 with a significance above 3σ (see Figure 1). The number of counts in an annular region of radii $2''$ and $30''$, centered on the radio core position, is 114, while those expected for the same region in the background is 45.4. The X-ray luminosity of the extended emission, L_X , estimated adopting an annular region of inner radius $2''$ and outer radius $30''$, centered on the location of 3CR 93, as previously done for 3CR 34, is $L_X = (2.3 \pm 0.5) \times 10^{43}$ erg s $^{-1}$.

3CR 107. This FR II—HERG radio galaxy lies at $z = 0.785$ (McCarthy et al. 1997). In our *Chandra* snapshot observation we clearly detected the nuclear emission as well as X-ray extended emission associated with the southern lobe (see Figure 3 and Table 5), as also indicated by the low value of the “ext ratio” in Table 3.

3CR 114. This FR II radio galaxy is at $z = 0.815$, showing fairly weak emission lines in its optical spectrum that led to a LERG classification (Strom et al. 1990). A faint compact nucleus with several clumps within the few arcseconds is observed at radio frequencies and a jet-like feature appears on the northern side in the 1.4 GHz image (Kharb et al. 2008), while single hotspots are detected both in the southern and in the northern lobes. Strom et al. (1990) claimed that this radio galaxy could lie in the core of a rich, distant cluster with some signatures of a merger, on the basis of their optical observations. In the X-ray image the nucleus is detected, but there is no evidence of hotspots and no signatures of X-ray emission from the intracluster medium were found.

3CR 142.1. This is a double radio source (i.e., FR II morphology) at $z = 0.4061$. In the radio there are two clear extended radio lobes with a radio bridge showing a constant

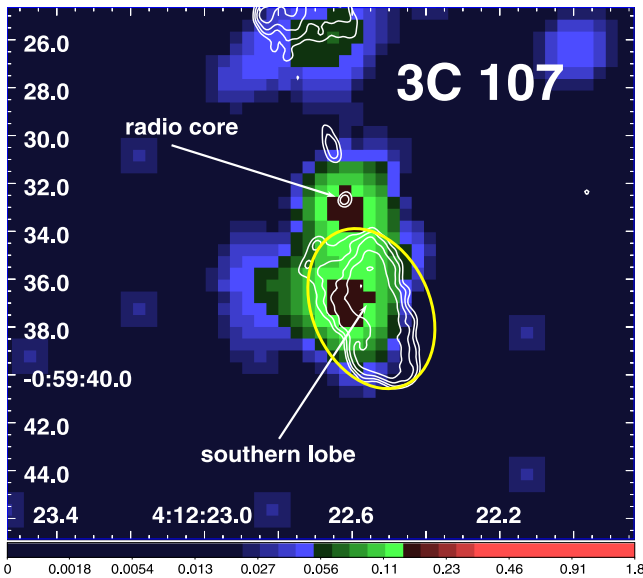


Figure 3. *Chandra* X-ray image for 3CR 107, centered on its southern lobe, in the energy range 0.5–7 keV. The image has been smoothed with a Gaussian function of 5-pixel kernel radius. Level radio contours (white) overlaid on the *Chandra* image were computed starting at 0.2 mJy/beam, increasing by a factor of 2 and drawn using the same 4.9 GHz radio map adopted for the registration. The X-ray flux of the southern lobe was measured using the yellow elliptical region drawn in the figure. Here there is spatial coincidence between the excess of X-ray photons and the lobe radio structure.

spectral index (Kharb et al. 2008; O’Dea et al. 2009). In the X-ray image only the radio nucleus is detected.

3CR 154. This is a nearby lobe-dominated quasar (Bogers et al. 1994) at $z = 0.58$ (Sokolovsky et al. 2011) appearing as a point-like source in the *HST* optical image. In the *Chandra* snapshot observation, only the relatively bright radio core is detected, for which X-ray spectral analysis was performed. As in 3CR 34 and 3CR 93, 3CR 154 shows extended X-ray emission on a kiloparsec scale, detected above the 5σ level of confidence, measured adopting the same method previously described (see Figure 1). We measured 243 X-ray photons in an annular region of radii $2''$ and $40''$, centered on the location of the radio core, while 70.1 are expected in the background region. This X-ray extended emission has a luminosity $L_X = (2.2 \pm 0.3) \times 10^{44} \text{ erg s}^{-1}$, measured using an annular region of inner radius $2''$ and outer radius $40''$, centered on the location of radio nucleus of 3CR 154. In the eastern lobe we found an association between the peak of the radio and the X-ray intensities for a radio knot lying at $33''$ from the nucleus (see marked region in Figure 4). Given this spatial coincidence, this excess of X-ray photons is probably due to the high-energy counterpart of the radio extended structure. On the other hand, the southern knot in the same eastern lobe does not show a correspondence between the radio and the X-ray emissions ($\sim 1''$ offset), indicating that this high-energy emission could be linked to the hot gas in the intergalactic medium.

3CR 169.1. This classical FR II radio galaxy is at $z = 0.633$. There is no detection of the jet and/or of the hotspots in the radio map at 8 GHz (Kharb et al. 2008). Harvanek & Hardcastle (1998) classified this source as a narrow emission line radio galaxy according to its optical spectrum. In the X-ray

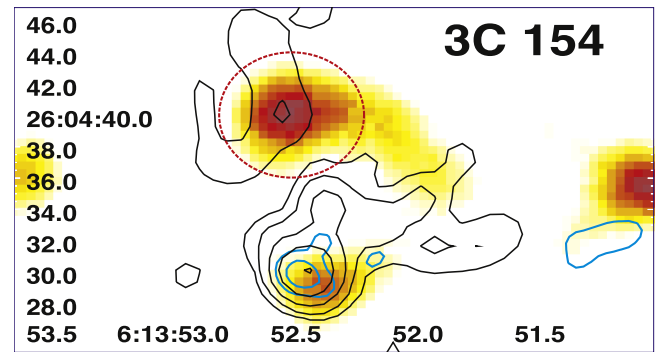


Figure 4. *Chandra* X-ray image for 3CR 154, centered on its eastern lobe, in the energy range 0.5–7 keV. The image has been smoothed with a Gaussian function of 8-pixel kernel radius. Radio contour levels, overlaid on the *Chandra* image, were computed using radio maps at 1.4 and at 8.46 GHz, starting at 1 and 2 mJy/beam and increasing by a factor of 2 and 4, respectively. A circular region of $4''$ radius, marked with a red dashed line, was used to measure the X-ray flux of the eastern knot. The southern radio knot, in the eastern lobe, has an offset of $1''$ between the peak of the radio surface brightness and the X-ray one. This second excess of X-ray photons could be due to diffuse hot gas in the large-scale environment.

snapshot image the nucleus is detected but there is no detection of the extended radio structure.

3CR 217. This is an FR II radio galaxy with narrow emission lines at $z = 0.898$. In the radio image at 8 GHz there are no jet signatures, in either the eastern or the western lobes (Mullin et al. 2008), and only the western lobe is detected. In the X-ray band the radio core is detected but the *Chandra* image is not registered because we were not able to precisely locate its position. Only a single photon is associated with the western hotspot being undetected in the X-rays.

3CR 225B. This is a FR II radio galaxy at $z = 0.582$, optically classified as a narrow emission line galaxy. It only shows hotspots within its radio lobes (Mullin et al. 2008). In the X-ray there is a hint of diffuse emission near the nucleus but no detection for the two hotspots. We note that the nearby radio source 3CR 225A is also in the field of view of the *Chandra* snapshot observation on a nearby CCD, but we did not detect any signature of X-ray emission arising from this radio object.

3CR 237. This is the only compact steep spectrum (CSS) radio source in our sample. It shows an FR II radio morphology and is at $z = 0.877$. The radio source size is less than $2''$ (i.e., less than ~ 15 kpc at $z = 0.877$) and it has a clear X-ray counterpart.

3CR 247. This is an FR II radio galaxy at $z = 0.75$, showing two hotspots on both the eastern and the western sides, optically classified as a narrow emission line radio galaxy. The host galaxy associated with the radio source 3CR247 lies in a very crowded field. In the *HST* optical image it appears as a symmetrical central galaxy with a close companion lying about 0.8 arcsec to the south. Two nearby galaxies also lie within the envelope of the infrared emission (see e.g., Best et al. 1998; Best 2000). Radio spectral aging analysis of this source has yielded an age of 3–5 million years, corresponding to a hotspot advance velocity of about $0.1c$ (Liu et al. 1992). In the *Chandra* X-ray image the radio core and the northern hotspot are detected.

3CR 272. This is a classical double FR II radio source at $z = 0.944$ showing a relatively faint nuclear component with

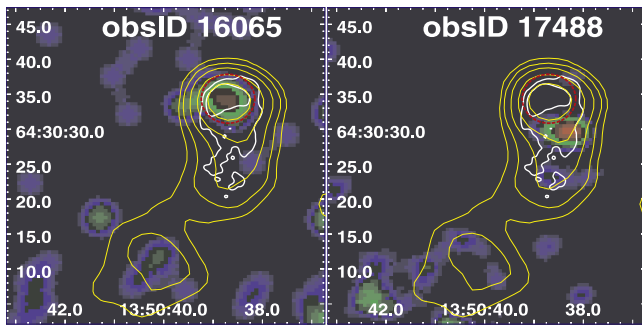


Figure 5. *Chandra* X-ray images for 3CR 292, centered on its northern lobe, in the energy range 0.5–7 keV. The left image corresponds to the *Chandra* observation with a shorter exposure time (obsID 16065, ~ 4 ks), while the right panel corresponds to the deeper one (obsID 17488 ~ 8 ks of exposure time). Both images have been smoothed with a Gaussian function of 8-pixel kernel radius. The five radio contours levels, yellow at 1.4 GHz and white at 8.5 GHz, overlaid on the *Chandra* image, were computed starting at 8 and 0.4 mJy/beam, increasing by a factor of 2 and 4, respectively. An elliptical region, marked with a red dashed line, was used to compute the X-ray flux of the northern lobe and it is also shown.

respect to the two hotspots at radio frequencies. Its optical spectrum shows a typical HERG spectrum with high ionization emission lines (Strom et al. 1990). There is nothing to report in the *Chandra* snapshot image other than the core detection.

3CR 277. This is a giant FR II radio galaxy at $z = 0.414$ (Strom et al. 1990), optically classified as a low excitation type radio galaxy (i.e., LERG). At 1.4 GHz, the core and a jet-like structure are detected in the eastern lobe. Both radio lobes show double hotspots in high-resolution radio images (see, e.g., Harvanek & Hardcastle 1998). According to McCarthy et al. (1997) the source reveals a basic double morphology, with the nuclear component slightly offset from the geometrical center. In the X-ray image the radio core is detected, while neither double hotspot has an X-ray counterpart.

3C 277.2. This FR II radio galaxy at $z = 0.767$ is optically classified as a narrow-line emission galaxy. It has a clear jet-like component in the southern lobe that is closer to the radio core but no signatures in the X-rays.

3CR 288.1. This is a lobe-dominated QSO lying at $z = 0.961$ with a clear point-like optical counterpart (Gendre & Wall 2008). In the X-ray image the nucleus is clearly detected and given the high number of photons with respect to the majority of the other targets, we also performed its spectral analysis, finding its X-ray spectrum to be consistent with an absorbed power law (see Table 4). Extended emission on a kiloparsec scale seems to be present around the core (see Table 3), but no evidence of a galaxy cluster or a group of galaxies is present in the optical images.

3CR 292. This is narrow-line FR II radio galaxy at redshift 0.713. Mullin et al. (2006) reported the detection of the two hotspots and the core in the radio map at 8.45 GHz but apart from the core, none of these features are detected in the X-rays. Adopting the same procedure as in previous cases, we found that 3CR 292 shows extended X-ray emission (more than 3σ detection significance) detected on a kiloparsec scale and potentially due to the presence of hot gas in the intergalactic medium (see Figure 1). The number of X-ray photons measured in an annular region of radii $2''$ and $75''$, centered on the radio core position, is 525, while those

expected in the background, for the same area, is 364.3, where both X-ray counts have been measured using the merged event file. We estimated an X-ray luminosity for the extended emission of $L_X = (2.5 \pm 0.7) \times 10^{44} \text{ erg s}^{-1}$, using the same annular region. Belsole et al. (2004) reported the X-ray detection of radio lobes in an *XMM-Newton* observation and as previously stated in the merged event file, we clearly detected an excess of X-ray photons corresponding to the location of the northern hotspot. However, as shown in Figure 5, in a circular region of $3''.5$ radius, centered on the northern hotspot, we measured 5 X-ray counts in the ~ 4 ks *Chandra* observation (i.e., obsID 16065), but only 1 in the deeper one (i.e., obsID 17488, ~ 8 ks exposure time). Then, in the latter observation, the peak of the radio surface brightness is not coincident with the X-ray excess. Since this radio structure lies in a large-scale environment permeated by X-ray emission from the hot intergalactic medium, we measured the level of the X-ray background of the ~ 4 ks observation within $75''$ from the radio core and excluding the nuclear X-ray emission. We found that, over the same area (i.e., circle of $3''.5$ radius), the expected number of counts is 1.5 ± 1.2 (obsID 16065), thus this X-ray excess is consistent with a 3σ fluctuation of the diffuse X-ray background. A deeper investigation will be necessary to distinguish between X-ray emission associated with the hotspot and that of the intergalactic medium. Variability on a monthly timescale has been excluded because the hotspot size, even if being relatively compact with respect to the lobe structure, covers a region of ~ 25 kpc.

3CR 293.1. This faint FR II radio galaxy is at $z = 0.709$. Its radio structures, i.e., the nucleus and both hotspots, are barely detected in the radio image available to us at 4.9 GHz and the comparison with the X-ray image indicates that the radio core is detected with possible extended X-ray emission around it (see Table 3).

3CR 323. This is a FR II radio galaxy at $z = 0.679$. McCarthy et al. (1997) pointed out that the outer lobes are irregular and rather different in structure, the northern one undergoing a sharp bend to the east and ending in what may be a hotspot. In the X-ray we only detected the nucleus and there is also significant X-ray extended emission surrounding it both on scales of few a tens and ~ 300 kpc (above 5σ significance), potentially due to its intergalactic medium (see Figure 1). There are 329 X-ray photons in an annular region of radii $2''$ and $75''$, centered on the radio core position, while 269.3 background photons are expected in this region. In this case the number of X-ray counts within a circular region of $2''$ positioned on two point-like sources lying on the western side of 3CR 323 were also subtracted from the X-ray photons measured within the annular region. This does not affect the significance of the detection of the X-ray extended emission since only 8 and 20 photons were measured for the 2 nearby objects. We estimated an X-ray luminosity of $L_X = (4.7 \pm 1.6) \times 10^{43} \text{ erg s}^{-1}$ for the extended emission surrounding 3CR 323; this was measured over an annular region of inner radius $2''$ and outer radius $21''$, centered on the location of its radio core. A lower value of the outer radius for the annular region has been chosen to avoid contamination due to the presence of nearby foreground/background X-ray point-like sources.

5. Summary and Conclusions

This paper presents the analysis of *Chandra* snapshot observations of a subsample of the extragalactic sources listed in the revised 3CR, previously lacking *Chandra* observations and observed during Cycle 15. This data set extends the current *Chandra* coverage of the 3CR extragalactic catalog up to redshift $z = 1.0$. The 3CR extragalactic sample includes 22 sources, listing 1 CSS source and 3 quasars (QSOs), while all the remaining sources are FR II radio galaxies. Of these targets, 19 lie at z in the range 0.5–1.0 plus 3C 93, 3CR 142.1, and 3CR 277. One additional target, 3CR 255A, lies in the *Chandra* field of view of a nearby source (i.e., 3CR 255B) observed during these Cycle 15 observations, but its radio core is not detected in the X-rays.

The main aims of the 3CR *Chandra* snapshot survey are: (i) to search for X-ray emission from jet knots, hotspots, and lobes; (ii) to study the nuclear emission of their host galaxies; and (iii) to investigate their environments at all scales, aiming to discover new galaxy groups/clusters via the X-ray emission of the intergalactic medium.

In the present work, the basic source parameters for the newly acquired *Chandra* data are presented. We created flux maps for all the X-ray snapshot observations and compared them with radio images to search for the high-energy counterparts of extended radio structures (i.e., jet knots, hotspots, lobes). We measured their X-ray intensities in three energy ranges, namely the soft, medium, and hard bands, for all radio cores and hotspots detected in the X-rays. Then, for the nuclei brighter than 400 X-ray photons, measured in a circular region of $2''$ radius in the 0.5–7 keV energy range, we also performed X-ray spectral analysis showing nuclear spectra that were all consistent with a simple power-law model, with an eventual mild intrinsic absorption in a single case.

We found X-ray emission arising from three hotspots in 3CR 41, 3CR 54, and 3CR 225B. We also report the discovery of extended X-ray emission, on a scale of tens of parsecs, around the radio nuclei of 3CR 107 and 3CR 293.1, with that of the former source being due to the X-ray counterpart of the southern radio lobe. Three sources in our sample are members of optically known galaxy groups/clusters: 3CR 41, 3CR 44, and 3CR 247. In the last two cases we did not detect X-ray emission arising from the intergalactic medium, while a marginal detection (i.e., 2σ) was found for 3CR 34. Moreover, we discovered extended X-ray emission on a scale of few hundreds of kiloparsecs around the radio structures of 3CR 93, 3CR 154, 3CR 292, and 3CR 323, all above 3σ significance. Then, for 3CR 154, we also detected the X-ray counterpart of a knot in the eastern radio lobe at $33''$ distance from the nucleus.

Finally, we highlight that a table summarizing the state-of-the-art of the X-ray (i.e., *Chandra* and *XMM-Newton*) observations carried out to date is reported at the end of the present manuscript (see Appendix B). *Chandra* detections are all based on both our current and previous analysis and represent an update with respect to previous works, while those regarding *XMM-Newton*, shown here for the first time, are only based on a literature search.

We thank the anonymous referee for useful comments that led to improvements in the paper. F. M. is indebted to M. Murgia for useful discussions. Support for this work was provided by the

National Aeronautics and Space Administration through the *Chandra* X-ray Center contract, and through *Chandra* Award Number PF-150128 issued by the *Chandra* X-ray Center, which is operated by the Smithsonian Astrophysical Observatory for and on behalf of the National Aeronautics Space Administration under contract NAS8-03060 (HRC). We are grateful to M. Hardcastle and C. C. Cheung for providing several radio images of the 3CR sources, while the remaining ones were downloaded from the NVAS²⁴ (NRAO VLA Archive Survey), NED²⁵ (Nasa Extragalactic Database), and from the DRAGN webpage.²⁶ This investigation is supported by the NASA grants GO1-12125A, GO2-13115X, and GO4-15097X. G.R.T. acknowledges support from the National Aeronautics and Space Administration (NASA) through Einstein Postdoctoral Fellowship Award Number PF-150128, issued by the *Chandra* X-ray Observatory Center, which is operated by the Smithsonian Astrophysical Observatory for and on behalf of NASA under contract NAS8-03060. This work was also supported by contributions of European Union, Valle D'Aosta Region and the Italian Minister for Work and Welfare. This work was partially supported by the Smithsonian Astrophysical Observatory. The National Radio Astronomy Observatory is operated by Associated Universities, Inc., under contract with the National Science Foundation. This research has made use of data obtained from the High-Energy Astrophysics Science Archive Research Center (HEASARC) provided by NASA's Goddard Space Flight Center; the SIMBAD database operated at CDS, Strasbourg, France; the NASA/IPAC Extragalactic Database (NED) operated by the Jet Propulsion Laboratory, California Institute of Technology, under contract with the National Aeronautics and Space Administration. We used TOPCAT²⁷ (Taylor 2005) for the preparation and manipulation of the tabular data and the images. SAOImage DS9 were used extensively in this work for the preparation and manipulation of the images. SAOImage DS9 was developed by the Smithsonian Astrophysical Observatory.

Facilities: VLA, MERLIN, CXO (ACIS).

Appendix A Images of the Sources

For all the 3CR sources in our sample, radio morphologies are shown here as contours superposed on the regridded/smoothed X-ray event files (see Figures 6–27). The full width half maximum (FWHM) of the Gaussian smoothing function and the binning factor are reported in the figure captions. X-ray event files were limited to the 0.5–7 keV band and rebinned to change the pixel size with a binning factor “ f ” (e.g., $f = 1/4$ produces pixels 4 times smaller than the native ACIS pixel of $0''.492$). The labels on the color bar for each X-ray map are in units of counts/pixel. We included in each caption also the radio brightness of the lowest contour, the factor (usually 2 or 4) by which each subsequent contour exceeds the previous one, the frequency of the radio map, and the FWHM of the clean beam. Figures appear so different from each other mainly because of the wide range in angular size of the radio sources.

²⁴ <http://archive.nrao.edu/nvas/>

²⁵ <http://ned.ipac.caltech.edu/>

²⁶ <http://www.jb.man.ac.uk/atlas/>

²⁷ <http://www.star.bris.ac.uk/~mbt/topcat/>

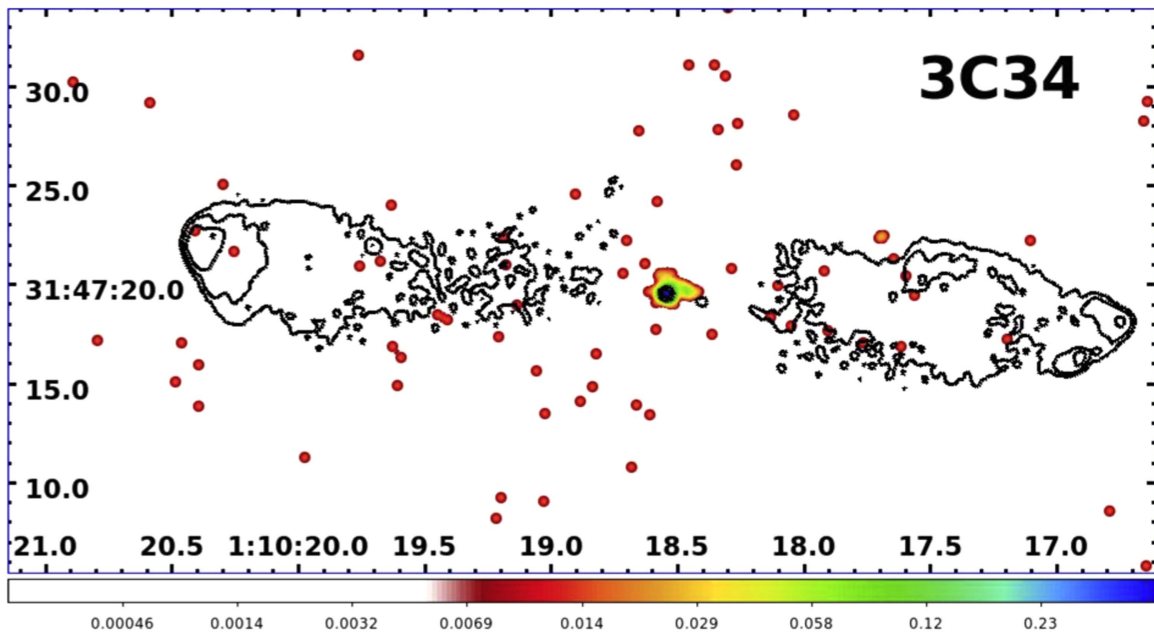


Figure 6. X-ray image of 3CR 34 for the energy band 0.5–7 keV. The event file has been regridded to 1/8 of the native pixel size (i.e., $0''.492$). The image has been smoothed with a Gaussian of $\text{FWHM} = 7''$. The radio contours (black) were computed using a 4.9 GHz radio map and start at 0.125 mJy/beam, increasing by factors of four.

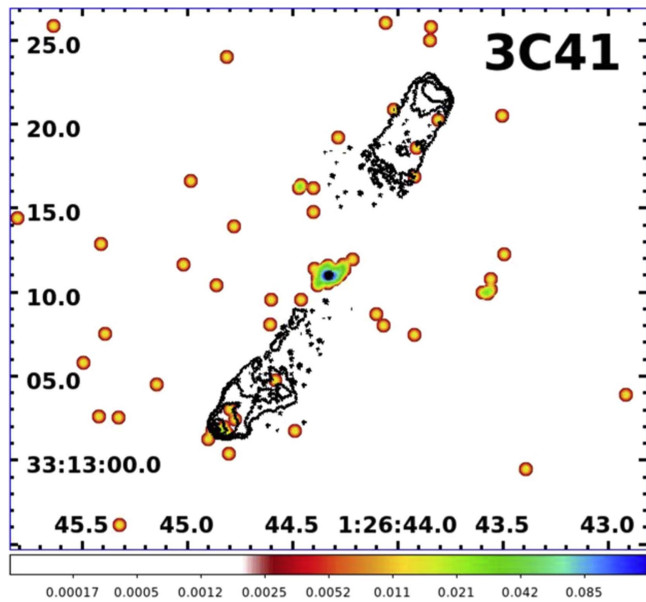


Figure 7. X-ray image of 3CR 41 for the energy band 0.5–7 keV. The event file has been regridded to 1/8 of the native pixel size (i.e., $0''.492$). The image has been smoothed with a Gaussian of $\text{FWHM} = 7''$. The radio contours (black) were computed using a 8.5 GHz radio map and start at 0.125 mJy/beam, increasing by factors of four.

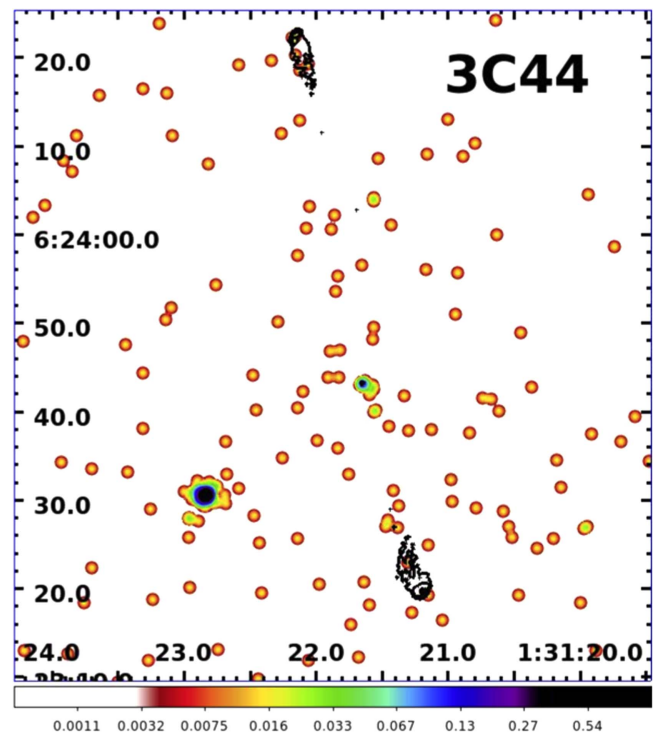


Figure 8. X-ray image of 3CR 44 for the energy band 0.5–7 keV. The event file has been regridded to 1/8 of the native pixel size (i.e., $0''.492$). The image has been smoothed with a Gaussian of $\text{FWHM} = 5''$. The radio contours (black) were computed using a 8.4 GHz radio map and start at 0.25 mJy/beam, increasing by factors of four. The radio core is weak but is detected in our 8.4 GHz radio image; thus, the *Chandra* image is registered.

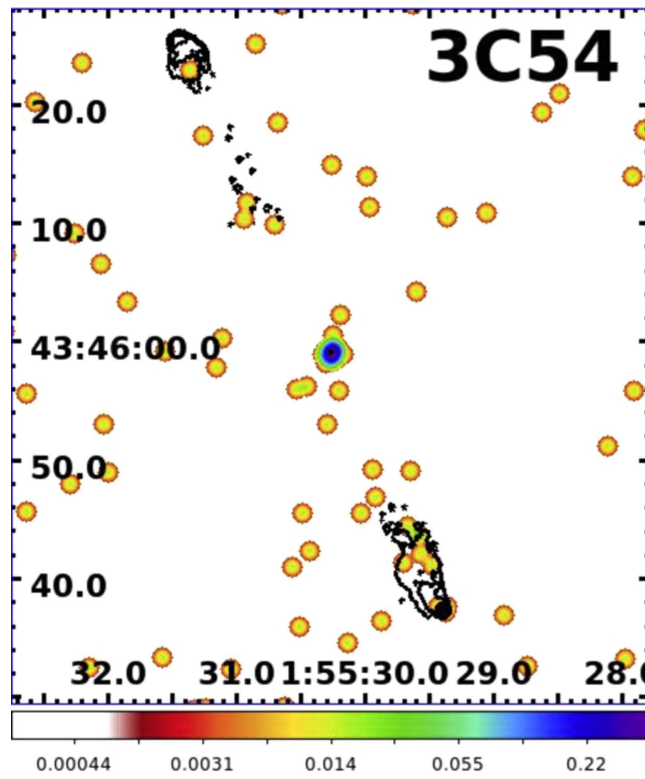


Figure 9. X-ray image of 3CR 54 for the energy band 0.5–7 keV. The event file has been regridded to 1/8 of the native pixel size (i.e., $0''.492$). The image has been smoothed with a Gaussian of $\text{FWHM} = 7''$. The radio contours (black) were computed using a 8.4 GHz radio map and start at 0.25 mJy/beam, increasing by factors of four.

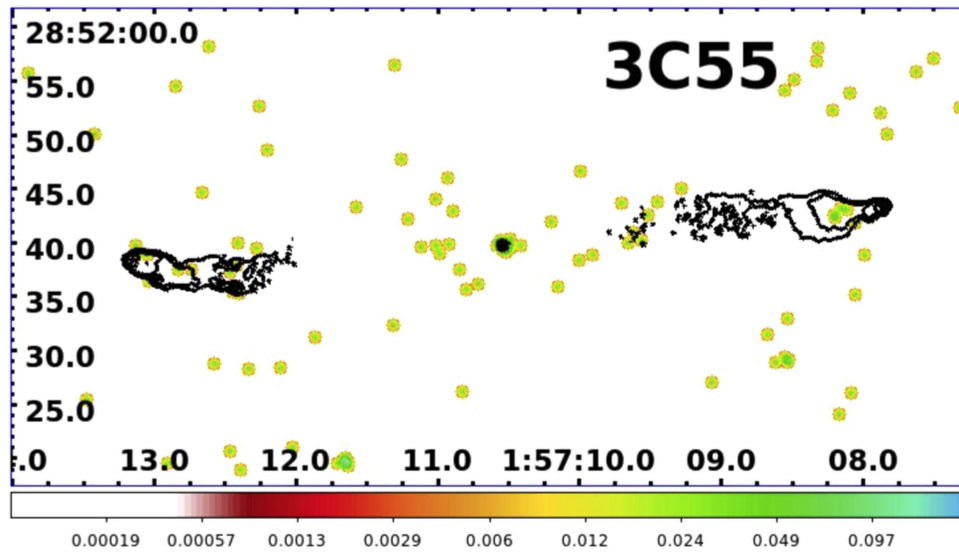


Figure 10. X-ray image of 3CR 55 for the energy band 0.5–7 keV. The event file has been regridded to 1/4 of the native pixel size (i.e., $0''.492$). The image has been smoothed with a Gaussian of $\text{FWHM} = 5''$. The radio contours (black) were computed using a 4.8 GHz radio map and start at 0.125 mJy/beam, increasing by factors of four.

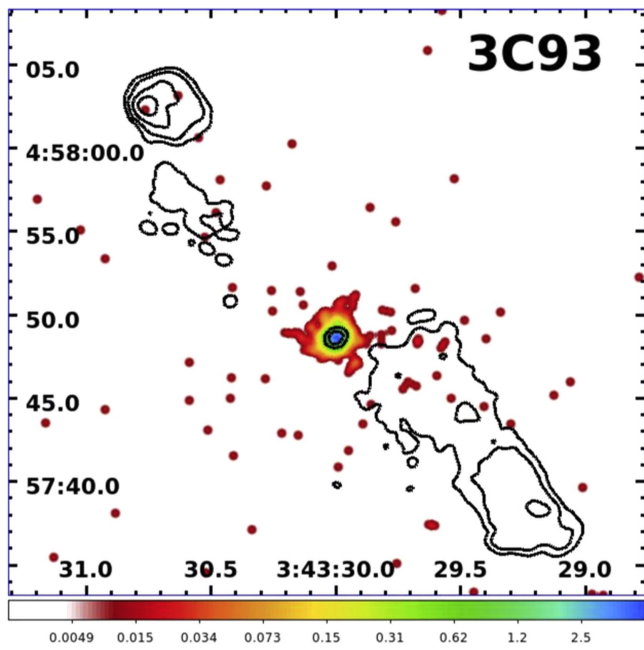


Figure 11. X-ray image of 3CR 93 for the energy band 0.5–7 keV. The event file has been regridded to 1/8 of the native pixel size (i.e., $0''.492$). The image has been smoothed with a Gaussian of $\text{FWHM} = 7''$. The radio contours (black) were computed using a 8.5 GHz radio map and start at 0.3 mJy/beam, increasing by factors of four.

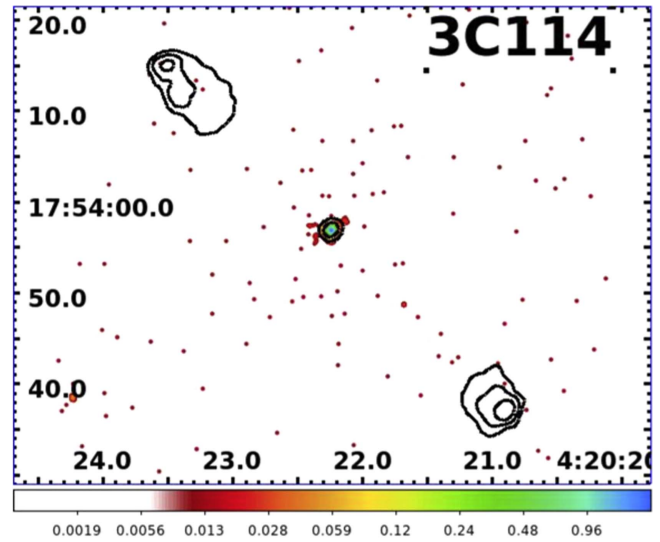


Figure 13. X-ray image of 3CR 114 for the energy band 0.5–7 keV. The event file has been regridded to 1/8 of the native pixel size (i.e., $0''.492$). The image has been smoothed with a Gaussian of $\text{FWHM} = 7''$. The radio contours (black) were computed using a 4.9 GHz radio map and start at 1.0 mJy/beam, increasing by factors of four.

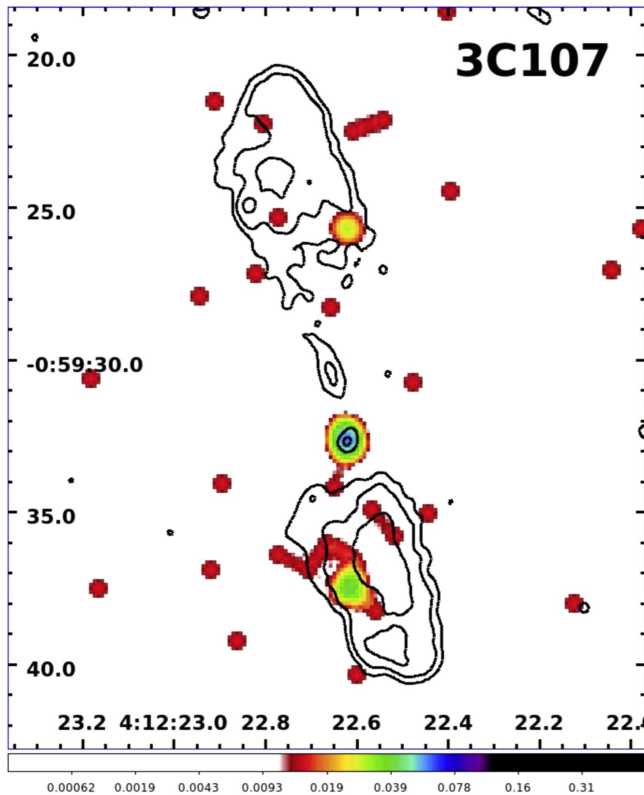


Figure 12. X-ray image of 3CR 107 for the energy band 0.5–7 keV. The event file has been regridded to 1/4 of the native pixel size (i.e., $0''.492$). The image has been smoothed with a Gaussian of $\text{FWHM} = 7''$. The radio contours (black) were computed using a 4.9 GHz radio map and start at 0.125 mJy/beam, increasing by factors of four.

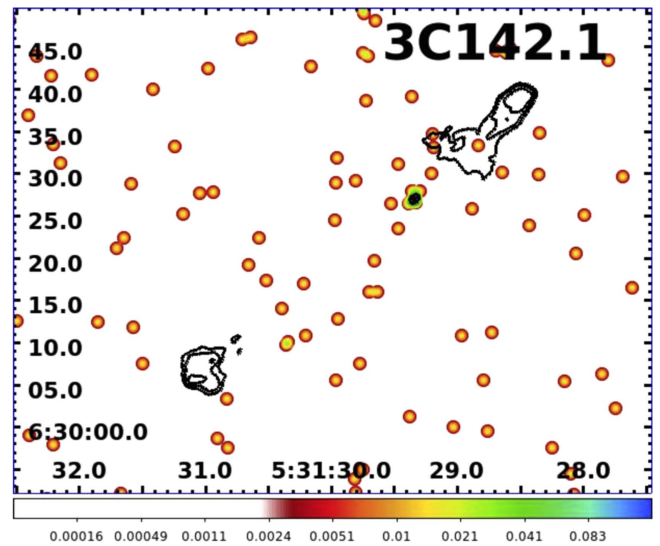


Figure 14. X-ray image of 3CR 142.1 for the energy band 0.5–7 keV. The event file has been regridded to 1/4 of the native pixel size (i.e., $0''.492$). The image has been smoothed with a Gaussian of $\text{FWHM} = 7''$. The radio contours (black) were computed using a 8.5 GHz radio map and start at 0.4 mJy/beam, increasing by factors of four.

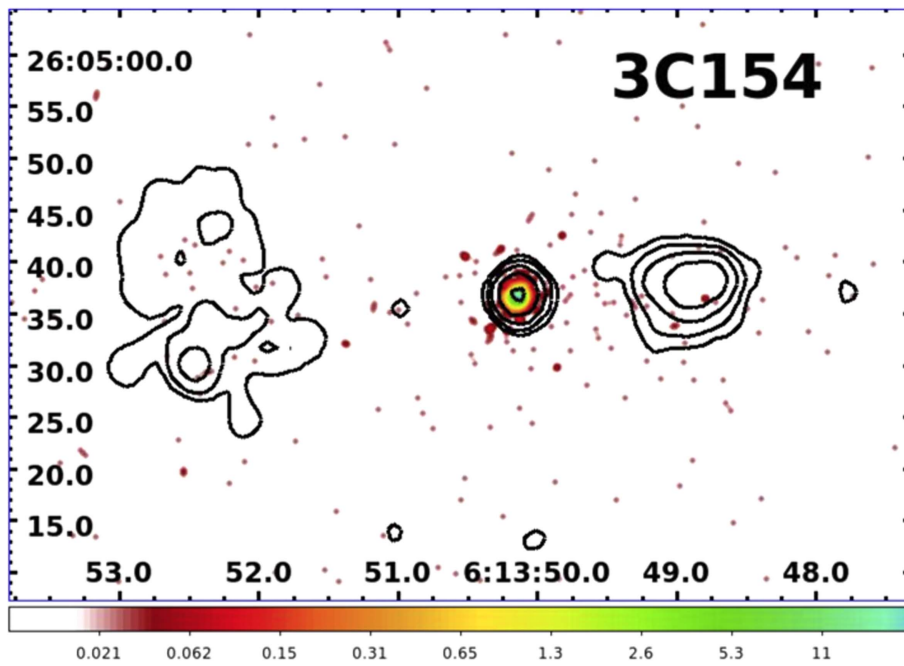


Figure 15. X-ray image of 3CR 154 for the energy band 0.5–7 keV. The event file has been regridded to 1/4 of the native pixel size (i.e., $0''.492$). The image has been smoothed with a Gaussian of $\text{FWHM} = 5''$. The radio contours (black) were computed using a 8.5 GHz radio map and start at 1 mJy/beam, increasing by factors of four.

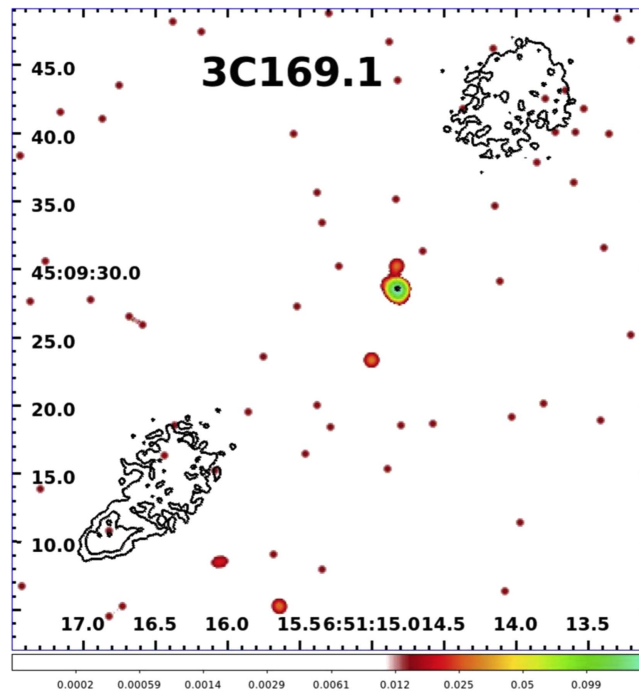


Figure 16. X-ray image of 3CR 169.1 for the energy band 0.5–7 keV. The event file has been regridded to 1/4 of the native pixel size (i.e., $0''.492$). The image has been smoothed with a Gaussian of $\text{FWHM} = 7''$. The radio contours (black) were computed using a 8.4 GHz radio map and start at 0.25 mJy/beam, increasing by factors of four.

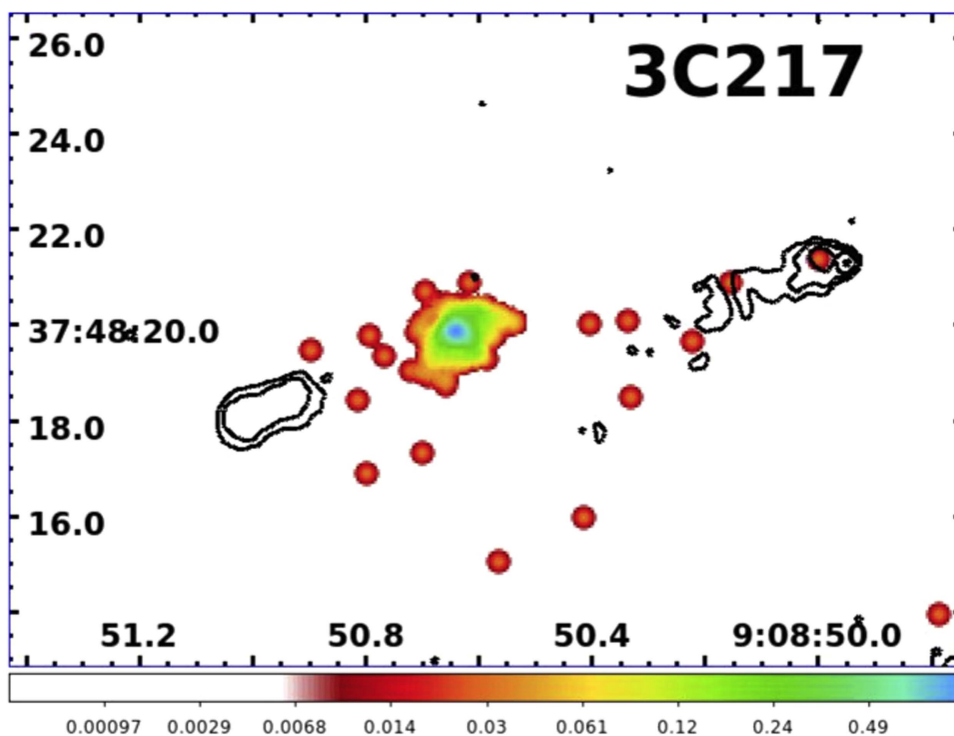


Figure 17. X-ray image of 3CR 217 for the energy band 0.5–7 keV. The event file has been regridded to 1/8 of the native pixel size (i.e., $0''.492$). The image has been smoothed with a Gaussian of $\text{FWHM} = 5''$. The radio contours (black) were computed using a 8.5 GHz radio map and start at 0.3 mJy/beam, increasing by factors of four. Since there is only a marginal detection of the radio nucleus, the X-ray image has not been registered.

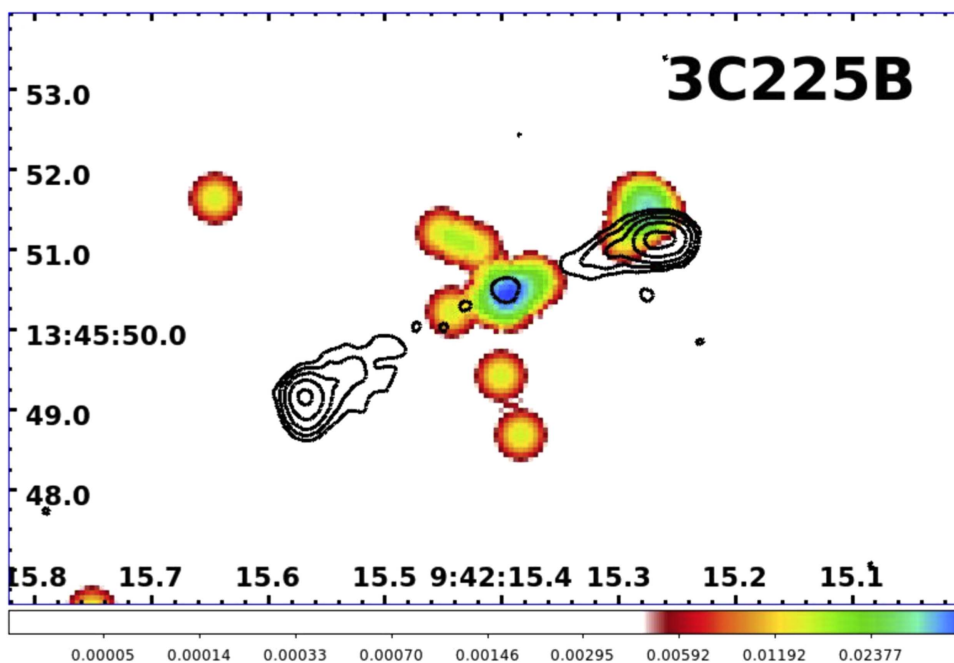


Figure 18. X-ray image of 3CR 225B for the energy band 0.5–7 keV. The event file has been regridded to 1/8 of the native pixel size (i.e., $0''.492$). The image has been smoothed with a Gaussian of $\text{FWHM} = 7''$. The radio contours (black) were computed using a 8.4 GHz radio map and start at 0.3 mJy/beam, increasing by factors of four.

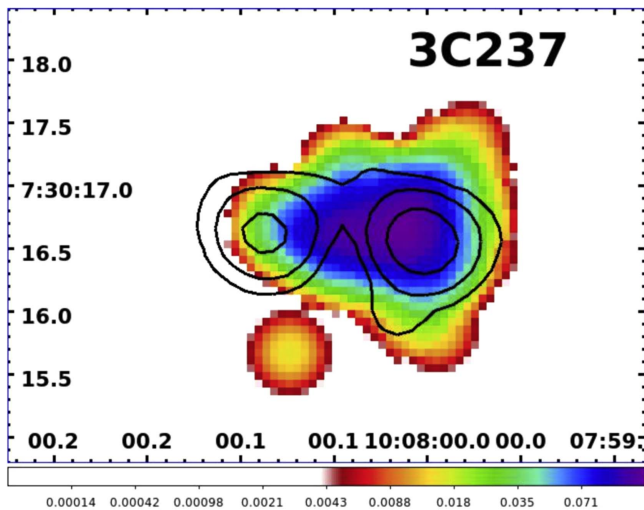


Figure 19. X-ray image of 3CR 44 for the energy band 0.5–7 keV. The event file has been regridded to 1/8 of the native pixel size (i.e., $0''.492$). The image has been smoothed with a Gaussian of $\text{FWHM} = 7''$. The radio contours (black) were computed using a 14.9 GHz radio map and start at 4.8 mJy/beam, increasing by factors of four. Given the small source size, the X-ray image has not been registered.

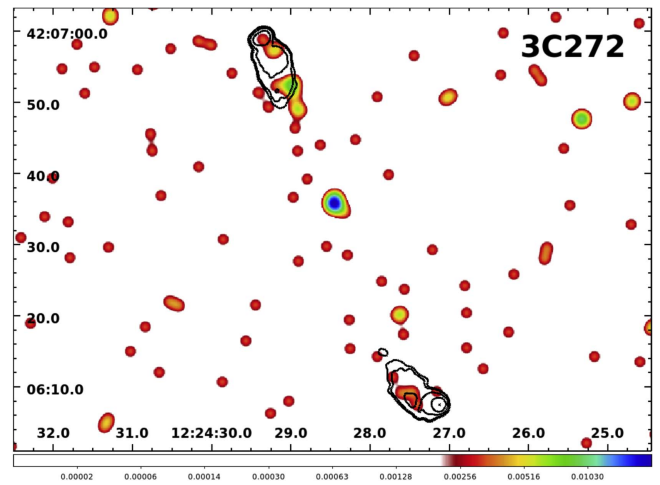


Figure 21. X-ray image of 3CR 272 for the energy band 0.5–7 keV. The event file has been regridded to 1/4 of the native pixel size (i.e., $0''.492$). The image has been smoothed with a Gaussian of $\text{FWHM} = 2''$. The radio contours (black) were computed using a 4.86 GHz radio map and start at 0.8 mJy/beam up to 0.08 Jy/beam. Since there is only a marginal detection of the radio nucleus, the X-ray image has not been registered.

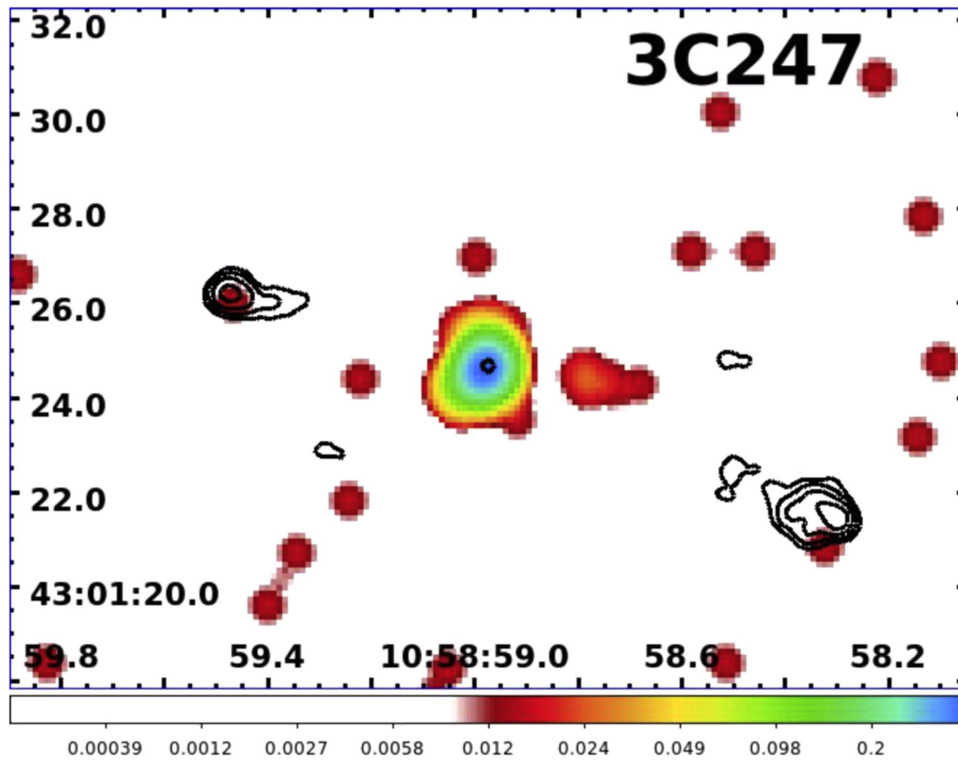


Figure 20. X-ray image of 3CR 247 for the energy band 0.5–7 keV. The event file has been regridded to 1/4 of the native pixel size (i.e., $0''.492$). The image has been smoothed with a Gaussian of $\text{FWHM} = 7''$. The radio contours (black) were computed using a 4.9 GHz radio map and start at 1.2 mJy/beam, increasing by factors of four.

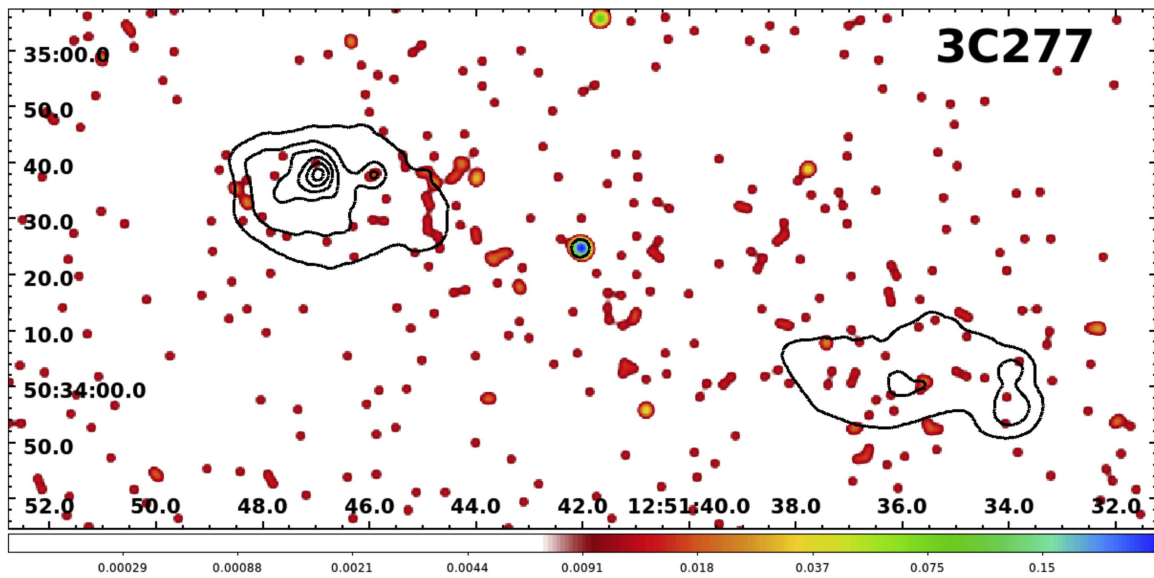


Figure 22. X-ray image of 3CR 277 for the energy band 0.5–7 keV. The event file has been regridded to $1/2$ of the native pixel size (i.e., $0''.492$). The image has been smoothed with a Gaussian of $\text{FWHM} = 2''$. The six radio contours (black) were computed using a 1.4 GHz radio map and start at 2 mJy/beam up to 0.08 Jy/beam (linear scale).

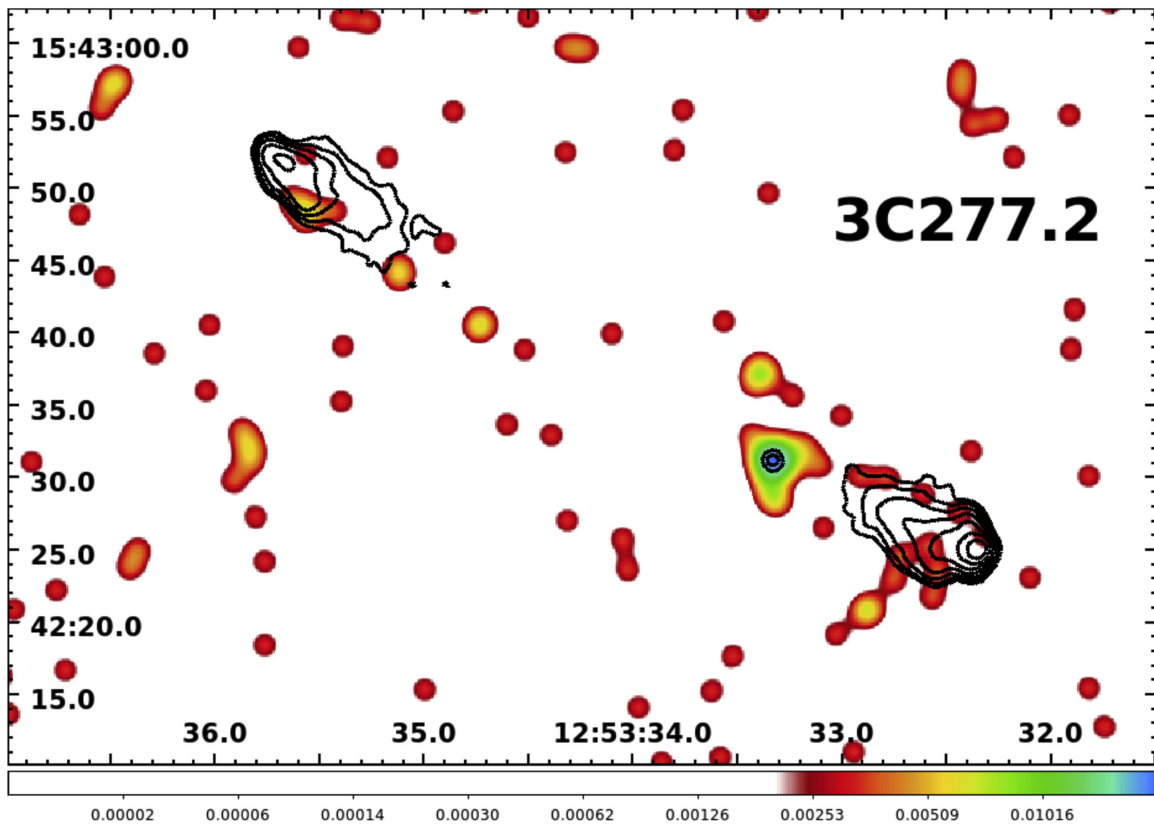


Figure 23. X-ray image of 3CR 277.2 for the energy band 0.5–7 keV. The event file has been regridded to $1/4$ of the native pixel size (i.e., $0''.492$). The image has been smoothed with a Gaussian of $\text{FWHM} = 2''$. The eight radio contours (black) were computed using a 1.4 GHz radio map and start at 0.2 mJy/beam up to 0.2 Jy/beam. Since there is only a marginal detection of the radio nucleus, the X-ray image has not been registered.

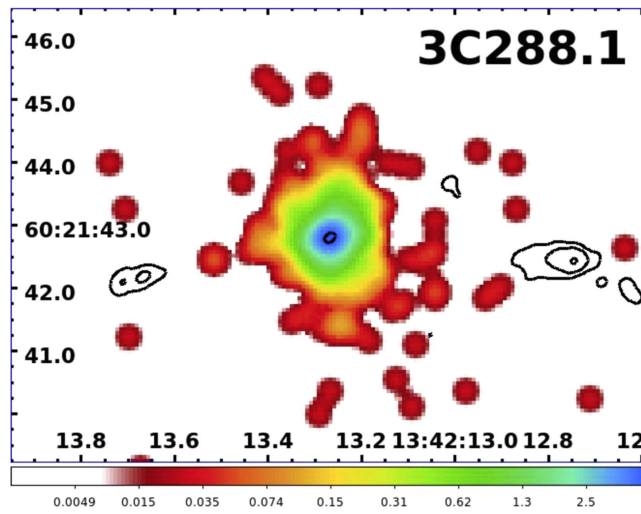


Figure 24. X-ray image of 3CR 288.1 for the energy band 0.5–7 keV. The event file has been regridded to 1/8 of the native pixel size (i.e., $0''.492$). The image has been smoothed with a Gaussian of FWHM = $5''$. The radio contours (black) were computed using a 8.4 GHz radio map and start at 2.0 mJy/beam, increasing by factors of four.

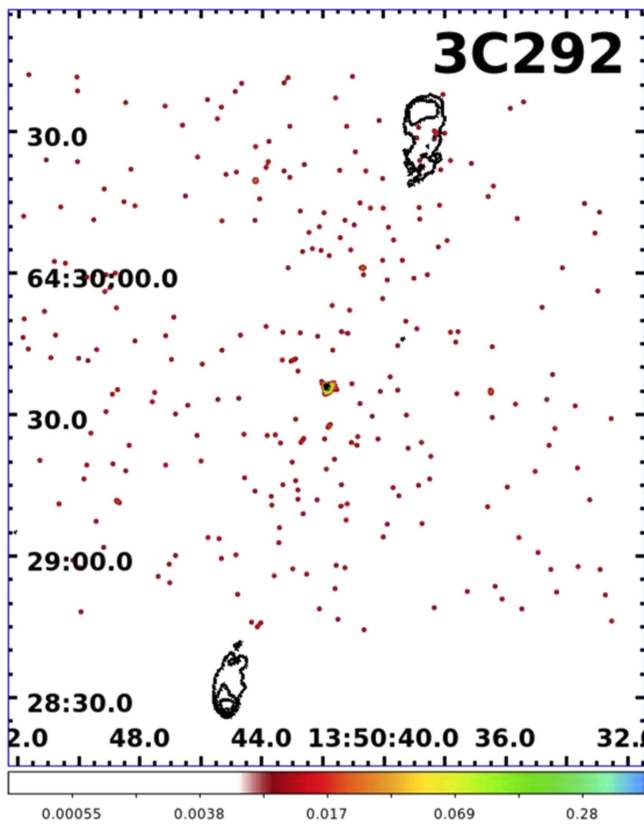


Figure 25. X-ray image of 3CR 292 for the energy band 0.5–7 keV (obsID 17488). The event file has been regridded to 1/4 of the native pixel size (i.e., $0''.492$). The image has been smoothed with a Gaussian of FWHM = $5''$. The radio contours (black) were computed using a 8.5 GHz radio map and start at 0.3 mJy/beam, increasing by factors of four.

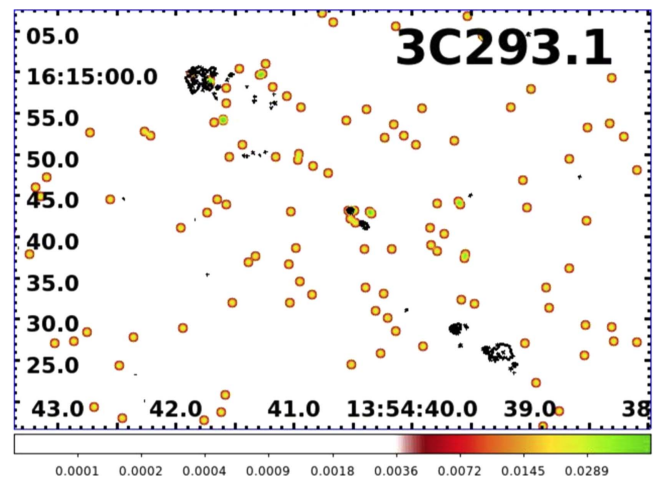


Figure 26. X-ray image of 3CR 292 for the energy band 0.5–7 keV. The event file has been regridded to 1/4 of the native pixel size (i.e., $0''.492$). The image has been smoothed with a Gaussian of FWHM = $5''$. The radio contours (black) were computed using a 4.9 GHz radio map and start at 0.15 mJy/beam, increasing by factors of two.

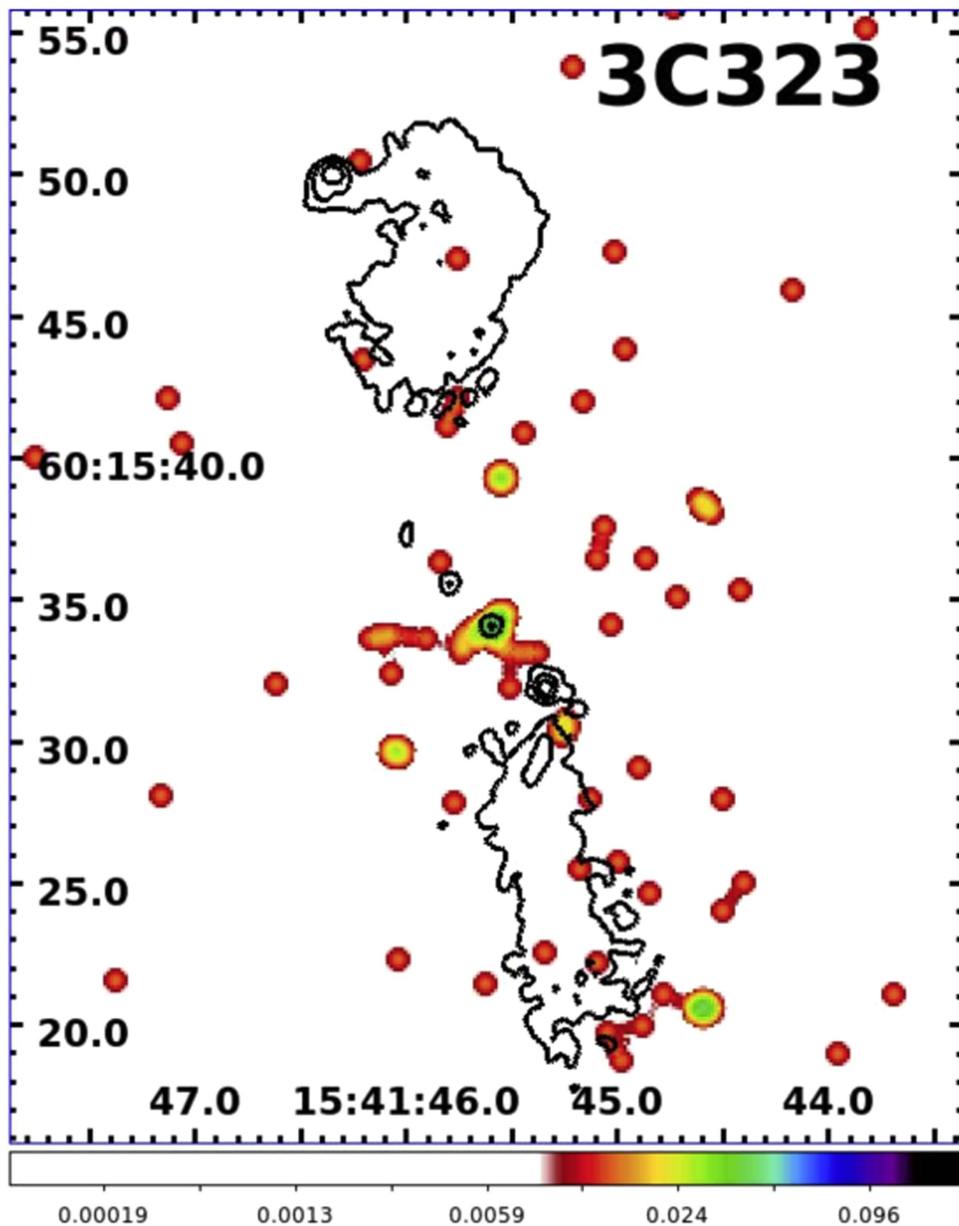


Figure 27. X-ray image of 3CR 292 for the energy band 0.5–7 keV. The event file has been regridded to 1/4 of the native pixel size (i.e., $0''.492$). The image has been smoothed with a Gaussian of $\text{FWHM} = 7''$. The radio contours (black) were computed using a 8.4 GHz radio map and start at 0.25 mJy/beam, increasing by factors of four.

Appendix B

The Status of the *Chandra* X-Ray 3CR Observations

Here, we present the current status of the *Chandra* and *XMM-Newton* observations for the entire 3CR catalog (see Table 6). While *Chandra* X-ray observations have been uniformly re-analyzed, as reported in our previous investigations, all the *XMM-Newton* information provided here is based on a literature search (see e.g., Croston et al. 2005; Belsole et al. 2007; Croston et al. 2008; Laskar et al. 2010; Shelton et al. 2011; Ineson et al. 2013; Mannering et al. 2013; Ineson et al. 2017, and references therein for more details).

For all 3CR sources, we report their classification using the following labeling: radio galaxies (RG), according to the Fanaroff & Riley criterion (Fanaroff & Riley 1974); quasars (i.e., QSRs); Seyfert galaxies (Sy), and BL Lac objects (BL). We also indicate as “UNID” those sources which, lacking

optical spectroscopy, remain unidentified. We include a column reporting the radio morphology for the radio galaxies (FR I versus FR II types) and indicating those objects that also show the radio structure of: (i) CSS or X-shaped (XS) radio sources or (ii) have been classified in the literature as wide-angle tailed or narrow-angle tailed radio galaxies (WAT and NAT, respectively). We also devoted a column to the optical classification of radio galaxies, distinguishing them as HERG or LERG. The most updated value of the redshift z is also reported and we used a “cluster flag” to label sources that belong to a known galaxy group/cluster. We considered sources belonging to a galaxy-rich large-scale environment those for which there is a known optical group/cluster reported in the literature and/or those for which there is an archival X-ray observation confirming the presence of hot gas in the intergalactic medium.

Table 6
The Current Status of the 3CR *Chandra* Observations

3CR Name	z	Class	Radio Morph.	Optical Class	Cluster Flag	<i>Chandra</i> Detections	<i>XMM-Newton</i> Detections	X-ray Obs.
2.0	1.03658	QSO	e	...	c
6.1	0.8404	RG	FRII	HERG	...	h	...	c
9.0	2.01976	QSO	LDQ	k;l	...	c
11.1	?	UNID	x
13.0	1.351	RG	FRII	HERG	...	e;h	...	c-x
14.0	1.469	QSO	c
14.1	?	UNID	x
15.0	0.07368	RG	FRI	LERG	...	k;l	...	c
16.0	0.405	RG	FRII	HERG	...	e;h;l	...	c-x
17.0	0.219685	QSO	k	...	c
18.0	0.188	RG	FRII	e	...	c
19.0	0.482	RG	FRII	LERG	yes	h;igm	...	c-x
20.0	0.174	RG	FRII	HERG	c-x
21.1	?	UNID	x
22.0	0.936	RG	FRII	c
27.0	0.184	RG	FRII	HERG	c
28.0	0.19544	RG	FRI	LERG	yes	igm	igm	c-x
29.0	0.045031	RG	FRI	LERG	yes	k;igm	...	c
31.0	0.017005	RG	FRI	LERG	yes	k	igm	c-x
33.0	0.0597	RG	FRII	HERG	yes	h;l	l;igm	c-x
33.1	0.181	RG	FRII	HERG	c
33.2	?	UNID	x
34.0	0.69	RG	FRII	HERG	yes	igm	...	c
35.0	0.067013	RG	FRII	LERG	yes	e;l	l;igm	c-x
36.0	1.301	RG	FRII	HERG	c
40.0	0.018	RG	FRI-WAT	LERG	yes	igm	igm	c-x
41.0	0.795	RG	FRII	HERG	...	h	...	c
42.0	0.39598	RG	FRII	HERG	c-x
43.0	1.459	QSO	CSS	c
44.0	0.66	QSO	yes	c
46.0	0.4373	RG	FRII	HERG	yes	...	igm	c-x
47.0	0.425	QSO	LDQ	h;l	...	c
48.0	0.367	QSO	CSS	c
49.0	0.23568	RG	FRII-CSS	HERG	c
52.0	0.29	RG	FRII-XS	HERG	yes	h	...	c
54.0	0.8274	RG	FRII	HERG	...	h	...	c
55.0	0.7348	RG	FRII	HERG	c-x
61.1	0.18781	RG	FRII	HERG	...	h	...	c-x
63.0	0.175	RG	FRII	HERG	c
65.0	1.176	RG	FRII	HERG	...	e;h	...	c-x
66.0A	?	BLL	BL	...	yes	c-x
66.0B	0.021258	RG	FRI-XS	LERG	yes	k	igm	c-x
67.0	0.3102	RG	FRII-CSS	c-x
68.1	1.238	QSO	c
68.2	1.575	RG	FRII	HERG	...	e;h	...	c
69.0	0.458	RG	FRII	HERG	c
71.0	0.003793	SEY	...	Sy2	c-x
75.0	0.023153	RG	FRI-WAT	LERG	yes	igm	igm	c-x
76.1	0.032489	RG	FRI	LERG	yes	igm	igm	c-x
78.0	0.028653	RG	FRI	LERG	...	k	...	c
79.0	0.2559	RG	FRII	HERG	yes	...	igm	c-x
83.1	0.025137	RG	FRI-NAT	LERG	yes	k;igm	igm	c-x
84.0	0.017559	RG	FRI	LERG	yes	igm	igm	c-x
86.0	?	UNID
88.0	0.030221	RG	FRI	LERG	yes	k;igm	igm	c-x
89.0	0.13981	RG	FRI-WAT	LERG	yes	igm	...	c
91.0	?	UNID
93.0	0.35712	QSO	e	...	c
93.1	0.243	RG	FRII-CSS	HERG	yes	c
98.0	0.030454	RG	FRII-XS	HERG	...	l	l	c-x
99.0	0.426	SEY	...	Sy2	c
103.0	0.33	RG	FRII	c
105.0	0.089	RG	FRII	HERG	...	k;h	...	c-x

Table 6
(Continued)

3CR Name	z	Class	Radio Morph.	Optical Class	Cluster Flag	<i>Chandra</i> Detections	<i>XMM-Newton</i> Detections	X-ray Obs.
107.0	0.785	RG	FRII	HERG	...	l	...	c
109.0	0.3056	RG	FRII	HERG	...	h;l	...	c-x
111.0	0.0485	RG	FRII	k;h	...	c-x
114.0	0.815	RG	FRII	LERG	c
119.0	1.023	QSO	CSS	c
123.0	0.2177	RG	FRII	LERG	yes	h;igm	...	c
124.0	1.083	RG	FRII	HERG	...	e	...	c
125.0	?	UNID	igm	...	c
129.0	0.0208	RG	FRI-NAT	...	yes	k;igm	igm	c-x
129.1	0.0222	RG	FRI	...	yes	igm	igm	c-x
130.0	0.109	RG	FRI-WAT	igm	...	c
131.0	?	UNID	c
132.0	0.214	RG	FRII	LERG	yes	c-x
133.0	0.2775	RG	FRII	HERG	c
134.0	?	UNID	c
135.0	0.12738	RG	FRII	HERG	yes	c
136.1	0.064	RG	FRII-XS	HERG	...	e	...	c
137.0	?	UNID	c
138.0	0.759	QSO	CSS	c
139.2	?	UNID	c
141.0	?	UNID	c
142.1	0.4061	RG	FRII	c
147.0	0.545	QSO	CSS	c
152.0	?	UNID	c
153.0	0.2769	RG	FRII	LERG	yes	c-x
154.0	0.58	QSO	e;k	...	c
158.0	?	UNID	c
165.0	0.2957	RG	FRII	LERG	...	e	...	c
166.0	0.2449	RG	FRII	LERG	c
169.1	0.633	RG	FRII	HERG	c
171.0	0.2384	RG	FRII	HERG	...	e	...	c-x
172.0	0.5191	RG	FRII	HERG	c
173.0	1.035	QSO	CSS	HERG	c
173.1	0.2921	RG	FRII	LERG	yes	h;l	...	c
175.0	0.77	QSO	c
175.1	0.92	RG	FRII	HERG	c
180.0	0.22	RG	FRII	HERG	c
181.0	1.382	QSO	h	...	c
184.0	0.994	RG	FRII	HERG	yes	l	igm	c-x
184.1	0.1182	RG	FRII	HERG	yes	c
186.0	1.06551	QSO	CSS	...	yes	igm	...	c
187.0	0.465	RG	FRII	LERG	...	e;l	...	c
190.0	0.24639	QSO	CSS	c
191.0	1.96810	QSO	k;l	...	c
192.0	0.05968	RG	FRII-XS	HERG	yes	l	igm	c-x
194.0	1.184	RG	FRII	HERG	c
196.0	0.87063	QSO	c
196.1	0.198	RG	FRII	LERG	yes	igm	...	c
197.1	0.12825	RG	FRII	HERG	yes	c
198.0	0.08145	RG	FRII	HERG	yes	c
200.0	0.458	RG	FRII	LERG	yes	k;l	...	c
204.0	1.112	QSO	c-x
205.0	1.53154	QSO	c-x
207.0	0.68038	QSO	LDQ	...	yes	k;l	igm	c-x
208.0	1.11151	QSO	c
208.1	1.02	QSO	c-x
210.0	1.169	RG	FRII	HERG	yes	e;h	igm	c-x
212.0	1.04931	QSO	LDQ	e;h	...	c
213.1	0.19405	RG	FRI-CSS	LERG	yes	e;h	...	c
215.0	0.41106	QSO	yes	k;l	...	c-x
216.0	0.67002	QSO	c
217.0	0.8975	RG	FRII	HERG	c
219.0	0.17456	RG	FRII	HERG	yes	k;l	...	c

Table 6
(Continued)

3CR Name	z	Class	Radio Morph.	Optical Class	Cluster Flag	<i>Chandra</i> Detections	<i>XMM-Newton</i> Detections	X-ray Obs.
220.1	0.61	RG	FRII	HERG	yes	igm	...	c
220.2	1.15610	QSO	h;l	...	c
220.3	0.68	RG	FRII	c
222.0	1.339	RG	FRI	c
223.0	0.13673	RG	FRII	HERG	yes	...	igm	c-x
223.1	0.1075	RG	FRII-XS	HERG	c
225.0A	1.565	RG	FRII	c
225.0B	0.58	RG	FRII	HERG	...	h	...	c
226.0	0.8177	RG	FRII	c
227.0	0.086272	RG	FRII	HERG	...	h	...	c
228.0	0.5524	RG	FRII	HERG	...	e;h	...	c
230.0	1.487	RG	FRII	HERG	c
231.0	0.000677	RG	FRI	LERG	c-x
234.0	0.184925	RG	FRII	HERG	...	h	...	c-x
236.0	0.1005	RG	FRII	LERG	c
237.0	0.877	RG	FRII-CSS	c
238.0	1.405	RG	FRII	HERG	c
239.0	1.781	RG	FRII	x
241.0	1.617	RG	FRII	c-x
244.1	0.428	RG	FRII	HERG	yes	e	...	c-x
245.0	1.027872	QSO	k	...	c
247.0	0.7489	RG	FRII	HERG	yes	c
249.0	1.554	QSO	x
249.1	0.3115	QSO	c-x
250.0	?	UNID
252.0	1.1	RG	FRII	c
254.0	0.736619	QSO	LDQ	e;h	...	c
255.0	1.355	QSO	c
256.0	1.819	RG	FRII	c
257.0	2.474	QSO	x
258.0	0.165	RG	FRI-CSS	LERG	yes	c
263.0	0.646	QSO	LDQ	h	...	c
263.1	0.824	RG	FRII	c
264.0	0.021718	RG	FRI	LERG	yes	k	igm	c-x
265.0	0.811	RG	FRII	h;l	...	c
266.0	1.275	RG	FRII	c-x
267.0	1.14	RG	FRII	c
268.1	0.97	RG	FRII	h	...	c
268.2	0.362	RG	FRII	...	yes	e;h	...	c-x
268.3	0.37171	RG	FRII	c
268.4	1.402200	QSO	c-x
270.0	0.007378	RG	FRI	LERG	yes	k	igm	c-x
270.1	1.528432	QSO	c
272.0	0.944	RG	FRII	c
272.1	0.003392	RG	FRI	LERG	yes	k	...	c-x
273.0	0.158339	QSO	CDQ	k	...	c-x
274.0	0.0043	RG	FRI	LERG	yes	k;igm	igm	c-x
274.1	0.422	RG	FRII	HERG	...	e	l	c-x
275.0	0.48	RG	FRII	LERG	yes	c
275.1	0.5551	QSO	LDQ	k;h;l	...	c
277.0	0.414	RG	FRII	c
277.1	0.31978	QSO	c
277.2	0.766	RG	FRII	HERG	c-x
277.3	0.085336	RG	FRII	HERG	c
280.0	0.996	RG	FRII	...	yes	k;h;l	...	c-x
280.1	1.667065	QSO	l	...	c
284.0	0.239754	RG	FRII	HERG	yes	...	igm	c-x
285.0	0.0794	RG	FRII	HERG	...	l	...	c
286.0	0.849934	QSO	c
287.0	1.055	QSO	c-x
287.1	0.2156	RG	FRII	HERG	...	h	...	c
288.0	0.246	RG	FRI	LERG	yes	igm	...	c
288.1	0.96296	QSO	c

Table 6
(Continued)

3CR Name	z	Class	Radio Morph.	Optical Class	Cluster Flag	<i>Chandra</i> Detections	<i>XMM-Newton</i> Detections	X-ray Obs.
289.0	0.9674	RG	FRII	c
292.0	0.71	RG	FRII	HERG	yes	e	igm	c-x
293.0	0.045034	RG	FRI	LERG	...	e	...	c
293.1	0.709	RG	FRII	c
294.0	1.779	RG	FRII	...	yes	h;igm	...	c
295.0	0.4641	RG	FRII	LERG	yes	h;igm	...	c
296.0	0.024704	RG	FRI	LERG	yes	k;igm	igm	c-x
297.0	1.4061	QSO	c
298.0	1.438120	QSO	yes	...	igm	c-x
299.0	0.367	RG	FRII	...	yes	h	...	c
300.0	0.27	RG	FRII	HERG	c-x
300.1	1.15885	RG	FRII	HERG	c
303.0	0.141186	RG	FRII	HERG	yes	k;l	...	c
303.1	0.2704	RG	FRII-CSS	HERG	...	e	...	c-x
305.0	0.041639	RG	FRII-CSS	HERG	...	e	...	c-x
305.1	1.132	RG	FRII-CSS	LERG	c
306.1	0.441	RG	FRII	HERG	yes	e	...	c
309.1	0.905	QSO	e	...	c
310.0	0.0538	RG	FRI	LERG	yes	igm	...	c
314.1	0.1197	RG	FRI	LERG	yes	c-x
313.0	0.461	RG	FRII	HERG	yes	h;igm	...	c
315.0	0.1083	RG	FRI-XS	LERG	yes	e	...	c
317.0	0.034457	RG	FRI	LERG	yes	igm	igm	c-x
318.0	1.574	RG	FRII	...	yes	c-x
318.1	0.045311	RG	FRI	...	yes	igm	igm	c-x
319.0	0.192	RG	FRII	LERG	yes	c-x
320.0	0.342	RG	FRII	...	yes	igm	...	c
321.0	0.0961	RG	FRII	HERG	...	h;l	...	c-x
322.0	1.681	RG	FRII	...	yes	...	igm	x
323.0	0.679	RG	FRII	e	...	c
323.1	0.2643	RG	FRII	HERG	yes	c
324.0	1.2063	RG	FRII	...	yes	e;h	...	c-x
325.0	1.135	RG	FRII	h	...	c
326.0	0.0895	RG	FRII	LERG	...	l	...	c
326.1	1.825	RG	FRII	c
327.0	0.1048	RG	FRII	HERG	yes	h	...	c
327.1	0.462	RG	FRI	HERG	...	k	...	c-x
330.0	0.55	RG	FRII	HERG	yes	h;l	...	c
332.0	0.151019	RG	FRII	HERG	yes	c
334.0	0.5551	QSO	LDQ	k;l	...	c
336.0	0.926542	QSO	c
337.0	0.635	RG	FRII	...	yes	e	...	c-x
338.0	0.030354	RG	FRI	LERG	yes	igm	igm	c-x
340.0	0.7754	RG	FRII	c
341.0	0.448	RG	FRII	HERG	yes	e;k	igm	c-x
343.0	0.988	QSO	c
343.1	0.75	RG	FRII	c
345.0	0.5928	QSO	CDQ	...	yes	k	igm	c-x
346.0	0.162012	RG	FRI	HERG	yes	k	...	c
348.0	0.155	RG	FRI	LERG	yes	igm	igm	c-x
349.0	0.205	RG	FRII	HERG	...	h	...	c-x
351.0	0.37194	RG	FRII	h	...	c
352.0	0.8067	RG	FRII	c
353.0	0.030421	RG	FRII	LERG	yes	k;l;igm	igm	c-x
356.0	1.079	RG	FRII	e	...	c
357.0	0.166148	RG	FRII	LERG	yes	c
368.0	1.131	RG	FRII	c
371.0	0.051	BLL	BL	k	...	c
379.1	0.256	RG	FRII	HERG	c
380.0	0.692	QSO	CDQ	k	...	c
381.0	0.1605	RG	FRII	HERG	c
382.0	0.05787	RG	FRII	HERG	c-x
386.0	0.016885	RG	FRI	LERG	yes	...	igm	c-x

Table 6
(Continued)

3CR Name	z	Class	Radio Morph.	Optical Class	Cluster Flag	<i>Chandra</i> Detections	<i>XMM-Newton</i> Detections	X-ray Obs.
388.0	0.0917	RG	FRII	LERG	yes	e	...	c
389.0	?	UNID	x
390.0	?	UNID	
390.3	0.0561	RG	FRII	HERG	...	k;h	...	c-x
394.0	?	UNID	
399.1	?	UNID	
401.0	0.2011	RG	FRII	LERG	yes	igm	...	c
402.0	0.025948	RG	FRI	...	yes	k	...	c-x
403.0	0.059	RG	FRII	HERG	...	k;h	...	c
403.1	0.0554	RG	FRII	LERG	yes	c
405.0	0.056075	RG	FRII	...	yes	h;igm	igm	c-x
409.0	?	UNID	
410.0	0.2485	RG	FRII	c
411.0	0.467	RG	FRII	HERG	c-x
415.2	?	UNID	
418.0	1.686	QSO	
424.0	0.126988	RG	FRI	LERG	yes	e	...	c
427.1	0.572	RG	FRII	LERG	yes	l;igm	...	c
428.0	?	UNID	
430.0	0.055545	RG	FRII	LERG	yes	e	...	c
431.0	?	UNID	
432.0	1.785	QSO	c-x
434.0	0.322	RG	FRII	...	yes	c
433.0	0.1016	RG	FRII	HERG	...	l	...	c
435.0	0.471	RG	FRII	c
436.0	0.2145	RG	FRII	HERG	...	e;h	...	c-x
437.0	1.48	RG	FRII	e;h	...	c
438.0	0.29	RG	FRII	HERG	yes	igm	...	c
441.0	0.708	RG	FRII	c
442.0	0.0263	RG	FRI	LERG	yes	igm	...	c
445.0	0.055879	RG	FRII	...	yes	h	...	c-x
449.0	0.017085	RG	FRI	LERG	yes	igm	igm	c-x
452.0	0.0811	RG	FRII	HERG	yes	h;l	igm	c-x
454.0	1.757	QSO	x
454.1	1.841	RG	FRII	...	yes	
454.2	?	UNID	
454.3	0.859	QSO	CDQ	k	...	c-x
455.0	0.543	QSO	c
456.0	0.233	RG	FRII	HERG	c
458.0	0.289	RG	FRII	HERG	yes	h	...	c
459.0	0.22012	RG	FRII	l	...	c-x
460.0	0.268	RG	FRII	LERG	yes	c-x
465.0	0.030221	RG	FRI-WAT	LERG	yes	k;igm	igm	c-x
468.1	?	UNID	
469.1	1.336	RG	FRII	l	c-x
470.0	1.653	RG	FRII	h	...	c

Note. Column (1): the 3CR name. Column (2): redshift z . We also verified in the literature (e.g., NED and/or SIMBAD databases) if new z values were reported after the release of the 3CR catalog. Column (3): the source classification of the sources: RG stands for radio galaxies, QSO stands for quasars, Sy stands for Seyfert galaxies, and BLL stands for BL Lac objects. We used the acronym UNID for sources that are still unidentified, i.e., they lack an optical spectroscopic observation. Column (4): the radio morphological classification; FR I and FR II refer to the Fanaroff and Riley classification criterion (Fanaroff & Riley 1974), while LDQ and CDQ are sometimes adopted for lobe-dominated and core-dominated quasars; we also indicated if in the literature the source is classified as CSS or if presents an X-shaped radio structure (XS) or if it is a narrow or wide-angle tailed radio galaxy (NAT and WAT, respectively). Column (5): the optical spectroscopic designation: LERG, “Low Excitation Radio Galaxy,” HERG, “High Excitation Radio Galaxy.” Column (6): the “cluster flag” as discussed in Appendix B. Column (7): in this column we report if the source has a radio component with an X-ray counterpart in a *Chandra* observation. We used the following labels: k = jet knot; h = hotspot; l = lobe; e = extended X-ray emission around the nucleus on kiloparsec scales and igm whenever this extended emission is associated with the hot gas present in the intergalactic medium. Column (8): the same as Column 7 but for the *XMM-Newton* observations. Column (9): The c flag indicates that at least one *Chandra* observation is present in its archive, while the x flag refers to the *XMM-Newton* archive.


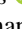
Regarding the X-ray analysis, we report X-ray detections of radio components, adopting the following symbols: k = jet knot; h = hotspot; l = lobe and igm for sources that belong to

a galaxy-rich large-scale environment. No distinction has been made between sources lying in groups or clusters of galaxies. We also adopt the symbol e for those radio objects that show

extended X-ray emission of on a kiloparsec scale as highlighted in our analyses using the “extent ratio” measurements. For *XMM-Newton* observations we only adopted *l* and *igm* symbols due to the lower angular resolution with respect to *Chandra* that does not allow us to see counterparts of jet knots and hotspots in the large fraction of the 3CR sources.

Finally, the “X-ray flag” indicates if the source was already observed by *Chandra* (c) and/or *XMM-Newton* (x). Sources marked with a * close to their 3CR name are those not re-analyzed in our previous studies (see Section 2 for more details). The table present in this work updates and thus supersedes those included in previous publications.

ORCID iDs

F. Massaro  <https://orcid.org/0000-0002-1704-9850>
 D. E. Harris  <https://orcid.org/0000-0002-2567-9449>
 R. P. Kraft  <https://orcid.org/0000-0002-0765-0511>
 A. Paggi  <https://orcid.org/0000-0002-5646-2410>
 G. R. Tremblay  <https://orcid.org/0000-0002-5445-5401>
 C. P. O’Dea  <https://orcid.org/0000-0001-6421-054X>
 B. J. Wilkes  <https://orcid.org/0000-0003-1809-2364>
 W. R. Forman  <https://orcid.org/0000-0002-9478-1682>

References

- Abdo, A. A., Ackermann, M., Ajello, M., et al. 2011, *ApJ*, 726, 43
 Baldi, R. D., Chiaberge, M., Capetti, A., et al. 2010, *ApJ*, 725, 2426
 Balmaverde, B., Capetti, A., Grandi, P., et al. 2012, *A&A*, 545A, 143
 Belsole, E., Worrall, D. M., Hardcastle, M. J., Birkinshaw, M., & Lawrence, C. R. 2004, *MNRAS*, 352, 924
 Belsole, E., Worrall, D. M., Hardcastle, M. J., & Croston, J. H. 2007, *MNRAS*, 381, 1109
 Bennett, A. S. 1962, *MmRAS*, 68, 163
 Bennett, C. L., Larson, D., Weiland, J. L., & Hinshaw, G. 2014, *ApJ*, 794, 135
 Best, P. N. 2000, *MNRAS*, 317, 720
 Best, P. N., Longair, M. S., & Ro’ ttering, H. J. A. 1997, *MNRAS*, 286, 785
 Best, P. N., Longair, M. S., & Ro’ ttering, H. J. A. 1998, *MNRAS*, 295, 549
 Blanton, E. L., Randall, S. W., Douglass, E. M., et al. 2009, *ApJ*, 697L, 95
 Bogers, W. J., Hes, R., Barthel, P. D., & Zensus, J. A. 1994, *A&A*, 105, 91
 Brinkman, A. C., Kaastra, J. S., van der Meer, R. L. J., et al. 2002, *A&A*, 396, 761
 Buttiglione, S., Capetti, A., Celotti, A., et al. 2009, *A&A*, 495, 1033
 Buttiglione, S., Capetti, A., Celotti, A., et al. 2011, *A&A*, 525A, 28
 Chiaberge, M., Gilli, R., Lotz, J. M., & Norman, C. 2015, *ApJ*, 806, 147
 Croston, J. H., Hardcastle, M. J., Birkinshaw, M., Worrall, D. M., & Laing, R. A. 2008, *MNRAS*, 386, 1709
 Croston, J. H., Hardcastle, M. J., Harris, D. E., et al. 2005, *ApJ*, 626, 733
 Dasadia, S., Sun, M., Morandi, A., et al. 2016, *MNRAS*, 458, 681
 Davis, J. E. 2001, *ApJ*, 562, 575
 Dicken, D., Tadhunter, C., Morganti, R., Axon, D., & Robinson, A. 2014, *ApJ*, 788, 98
 Edge, D. O., Shakeshaft, J. R., McAdam, W. B., Baldwin, J. E., & Archer, S. 1959, *MmRAS*, 68, 37
 Evans, D. A., Worrall, D. M., Hardcastle, M. J., Kraft, R. P., & Birkinshaw, M. 2006, *ApJ*, 642, 96
 Fabian, A. C., Sanders, J. S., Allen, S. W., et al. 2003, *MNRAS*, 344L, 43
 Fanaroff, B. L., & Riley, J. M. 1974, *MNRAS*, 167, P31
 Gendre, M. A., & Wall, J. V. 2008, *MNRAS*, 390, 819
 Giovannini, G., Taylor, G. B., Feretti, L., et al. 2005, *ApJ*, 618, 635
 Griffiths, R. E., Ptak, A., Feigelson, E. D., et al. 2000, *Sci*, 290, 1325
 Grimes, J. A., Rawlings, S., & Willott, C. J. 2004, *MNRAS*, 349, 503
 Haas, M., Willner, S. P., Heymann, F., et al. 2008, *ApJ*, 688, 122
 Hardcastle, M. J., Evans, D. A., & Croston, J. H. 2006, *MNRAS*, 370, 1893
 Hardcastle, M. J., Massaro, F., & Harris, D. E. 2010, *MNRAS*, 401, 2697
 Hardcastle, M. J., Massaro, F., Harris, D. E., et al. 2012, *MNRAS*, 424, 1774
 Hardcastle, M. J., & Worrall, D. M. 2000, *MNRAS*, 314, 359
 Harvanek, M., Ellingson, E., Stocke, J. T., & Rhee, G. 2001, *AJ*, 122, 2874
 Harvanek, M., & Hardcastle, M. J. 1998, *ApJS*, 119, 1
 Hes, R., Barthel, P. D., & Fosbury, R. A. E. 1996, *A&A*, 313, 423
 Hewitt, A., & Burbidge, G. 1991, *ApJS*, 75, 297
 Hilbert, B., Chiaberge, M., Kotyla, J. P., et al. 2016, *ApJS*, 225, 12
 Hiltner, P. R., & Roeser, H.-J. 2009, *ApJS*, 184, 398
 Ho, L. C., & Minjin, K. 2009, *ApJS*, 184, 398
 Ineson, J., Croston, J. H., Hardcastle, M. J., et al. 2013, *ApJ*, 770, 136
 Ineson, J., Croston, J. H., Hardcastle, M. J., & Mingo, B. 2017, *MNRAS*, 467, 1586
 Kalberla, P. M. W., Burton, W. B., Hartmann, D., et al. 2005, *A&A*, 440, 775
 Kharb, P., O’Dea, C. P., Baum, S. A., et al. 2008, *ApJS*, 174, 74
 Kuraszkievicz, J., et al. 2017, *ApJ*, submitted
 Laing, R. A., Riley, J. M., & Longair, M. S. 1983, *MNRAS*, 204, 151
 Laskar, T., Fabian, A. C., Blundell, K. M., & Erlund, M. C. 2010, *MNRAS*, 401, 1500
 Lehnert, M. D., Miley, G. K., Sparks, W. B., et al. 1999, *ApJS*, 123, 351L
 Leipski, C., Haas, M., Willner, S. P., et al. 2010, *ApJ*, 717, 766
 Liu, R., Pooley, G., & Riley, J. M. 1992, *MNRAS*, 257, 545
 Madrid, J. P., Chiaberge, M., Floyd, D., Sparks, W. B., & Macchetto, D. 2006, *ApJS*, 164, 307
 Mannerling, E., Worrall, D. M., & Birkinshaw, M. 2013, *MNRAS*, 431, 858
 Maselli, A., Massaro, F., Cusumano, G., et al. 2016, *MNRAS*, 460, 3829
 Massaro, F., Chiaberge, M., Grandi, P., et al. 2009a, *ApJL*, 692, L123
 Massaro, F., Harris, D. E., & Cheung, C. C. 2011, *ApJS*, 197, 24
 Massaro, F., Harris, D. E., Chiaberge, M., et al. 2009b, *ApJ*, 696, 980
 Massaro, F., Harris, D. E., Liuzzo, E., et al. 2015, *ApJS*, 220, 5
 Massaro, F., Harris, D. E., Tremblay, G. R., et al. 2010, *ApJ*, 714, 589
 Massaro, F., Tremblay, G. R., Harris, D. E., et al. 2012, *ApJS*, 203, 31
 Massaro, F., Harris, D. E., Tremblay, G. R., et al. 2013, *ApJS*, 206, 7
 McCarthy, P. J., Miley, G. K., de Koff, S., et al. 1997, *ApJS*, 112, 415
 McCarthy, P. J., Spinrad, H., & van Breugel, W. 1995, *ApJS*, 99, 27
 Mullin, L. M., Hardcastle, M. J., & Riley, J. M. 2006, *MNRAS*, 372, 113
 Mullin, L. M., Riley, J. M., & Hardcastle, M. J. 2008, *MNRAS*, 390, 595
 Nulsen, P. E. J., Hambrick, D. C., & McNamara, B. R. 2005, *ApJ*, 625L, 9
 O’Dea, C. P., Daly, R. A., Kharb, P., Freeman, K. A., & Baum, S. A. 2009, *A&A*, 494, 471
 Perryman, M. A. C., Lilly, S. J., Longair, M. S., & Downes, A. J. B. 1984, *MNRAS*, 209, 159
 Podigachoski, P., Barthel, P. D., Haas, M., et al. 2015, *A&A*, 575A, 80
 Privon, G. C., O’Dea, C. P., Baum, S. A., Axon, D. J., & Kharb, P. 2008, *ApJS*, 175, 423
 Shelton, D. L., Hardcastle, M. J., & Croston, J. H. 2011, *MNRAS*, 418, 811
 Siemiginowska, A., Burke, D. J., Aldcroft, Thomas L., et al. 2010, *ApJ*, 722, 102
 Sokolovsky, K. V., Kovalev, Y. Y., Pushkarev, A. B., & Lobanov, A. P. 2011, *A&A*, 532, 38
 Spinrad, H., Marr, J., Aguilar, L., & Djorgovski, S. 1985, *PASP*, 97, 932
 Stuardi, C., Missaglia, V., Massaro, F., et al. 2017, *ApJS*, submitted
 Strom, R. G., Riley, J. M., Spinrad, H., et al. 1990, *A&A*, 227, 19
 Taylor, M. B. 2005, in ASP Conf. Ser. 347, *Astronomical Data Analysis Software and Systems XIV.*, ed. P. Shopbell, M. Britton, & R. Ebert (San Francisco, CA: ASP), 29
 Tremblay, G. R., Chiaberge, M., Sparks, W. B., et al. 2009, *ApJS*, 183, 278
 Werner, M. W., Murphy, D. W., Livingston, J. H., Gorjian, V., & Jones, D. L. 2012, *ApJ*, 759, 86
 Westhues, C., Haas, M., Barthel, P., et al. 2016, *AJ*, 151, 120
 Wilkes, B. J., Kuraszkievicz, J., Haas, M., et al. 2013, *ApJ*, 773, 15